# Progress on heat and moisture recovery with membranes: From fundamentals to engineering applications ☆

Li-Zhi Zhang *

*Key Laboratory of Enhanced Heat Transfer and Energy Conservation of Education Ministry, School of Chemistry and Chemical Engineering, South China University of Technology, Guangzhou 510640, China*

## ARTICLE INFO

## ABSTRACT

Energy consumption by air conditioning accounts for 1/3 of the total energy use by the whole society. Cooling and dehumidifying fresh ventilation air constitutes 20–40% of the total energy load for air conditioning in hot and humid regions. Heat and moisture recovery from ventilation air has become a hot topic for building energy conservation in these years. Of the various technologies for heat and moisture recovery, membrane-based total heat exchanger is a promising alternative. Over the past 10 years, much work has been conducted in South China University of Technology for the research on membrane-based heat and moisture recovery, from fundamentals to engineering applications. In this review, the progress of these researches is introduced. More specifically, some novel concepts are proposed for heat and moisture transfer analysis. Several novel membranes are designed to accomplish the goal. Some novel exchanger structures are constructed and the heat and mass transport phenomena is investigated. Novel prototypes are built for engineering applications. The results are that a sensible effectiveness of 0.8 and a latent effectiveness of 0.7 are obtained for a total heat exchanger with novel materials and new constructions. When the total heat exchanger is combined with a fresh air refrigeration dehumidification unit, the system COP is improved to 5.8. The membrane systems have been extended to other areas like air humidification, liquid desiccant air dehumidification, and fabrication of selective adsorbents. This review gives a summary of these works and also points out the future research directions.

© 2012 Elsevier Ltd. All rights reserved.

## 1. Introduction

Indoor air quality has gained much attention recently [1–6]. Sufficient fresh air supply by ventilation is necessary for occupant's health. The obvious way to get more fresh air is to open a window. After all, that is one reason to put windows in buildings in the first place. However opening a window subverts the reason that the building is insulated in the first place. Energy conservation is of equal importance. Sensible and latent load accompanying the incoming fresh air is heavy. In hot and humid regions like Guangdong, conditioning fresh air represents 20–40% of the total load for air conditioning. It is thus significant to recover the cool and dryness from the exhaust air stream in summer [7–11].

Heat and moisture recovery, or the so called total heat exchangers, could save a large fraction of energy that is used for cooling and dehumidifying the fresh air. In fact, it is found that 70–90% of the energy for fresh air treatment can be saved [7,11]. With heat and moisture recovery, the efficiency of an existing HVAC system can also be improved. The reason is that traditionally the fresh air is dehumidified by cooling coil condensation and the subsequent re-heating processes, which are very energy intensive. On the other hand, this part of energy can be saved if heat and moisture recovery equipments are installed to reduce the dehumidification load. As a result, the cooling coil condensation can be prevented. In addition, the total heat exchangers are helpful for the prevention of epidemic respiratory diseases like SARS, H1N1, and Bird flu. Without them, people tend to close the windows to save energy, which generates a good environment for disease transmission.

There are various technologies to realize heat and moisture recovery: sensible-only heat exchangers or heat recuperators [12–14], heat pipes [15], energy wheels [16–24], run-around systems [25,26], liquid desiccant systems [5,6,27], solid desiccant systems [28,29], phase change materials [30], and membrane-based total heat exchangers [31–36]. Of the various technologies, membrane total heat exchangers has some advantages: (1) it has no cross-over problems; (2) it is stand still and have no moving parts; (3) it is simple; (4) its performance deteriorates little over time; (5) it is compact and high efficient. With this technology, both the sensible and the latent effectiveness can be as high as 0.9. Due to these reasons, it has attracted much attention in recent years.

## Nomenclature

| | |
|---|---|
| $a$ | half channel pitch or half fin height (m) |
| $A$ | area (m²) |
| $c_p$ | specific heat of air (kJ kg⁻¹ K⁻¹) |
| $C_1$ | constant in sorption curve |
| COP | coefficient of performance |
| $d_h$ | hydrodynamic diameter (m) |
| $D$ | diffusivity (m²/s) |
| $D_0$ | diameter of the module shell (m) |
| $D_f$ | area dimension |
| $D_t$ | tortuosity dimension |
| $f$ | friction factor |
| $h$ | convective heat transfer coefficient (kW m⁻² K⁻¹) |
| $J$ | permeation rate (kg m⁻² s⁻¹) |
| $k$ | convective mass transfer coefficient (m/s) |
| $K$ | overall mass transfer coefficient (m/s) |
| $k_p$ | partition coefficient |
| $L$ | length (m) |
| $Le$ | Lewis number |
| $l_s$ | length of the characteristic space (m) |
| $\dot{m}$ | mass flow arte (kg/s) |
| $N$ | number |
| $NTU$ | Number of Transfer Units |
| Nu | Nusselt number |
| $P$ | pressure (Pa) |
| $P_a$ | atmospheric pressure (101,325 Pa) |
| $p_m$ | mean partial pressure of vapor in pores (Pa) |
| Pe | permeability (m²) |
| Pe′ | permeability coefficient (g/(cm² s cm Hg)) |
| Pr | Prandtl number |
| $q$ | heat flux (kW/m²) |
| $r$ | resistance, (m² K/kW) for heat and (s/m) for mass |
| $R$ | gas constant, 8.314 J/(mol K) |
| Re | Reynolds number |
| Sc | Schmidt number |
| Sh | Sherwood number |
| $T$ | temperature (K) |
| $u$ | velocity (m/s) |
| $U$ | total heat transfer coefficient (kW m⁻² K⁻¹) |
| $V$ | flow rate (m³/h) |
| $w_{max}$ | maximum water uptake in membrane materials (kg/kg) |
| $x, y, z$ | coordinates (m) |
| $z_0$ | distance from water to membrane (m) |

*Greek letters*

| | |
|---|---|
| $\varepsilon$ | effectiveness |
| $\beta$ | nonuniformity parameter |
| $\theta$ | performance deterioration factor |
| $\phi$ | relative humidity |
| $\alpha$ | thermal diffusivity (m²/s) |
| $\varphi_1$ | packing fraction in hollow fiber module |
| $\tau$ | tortuosity |
| $\tau_0$ | membrane to fluid conductivity ratios |
| $\tau_1$ | duct aspect ratio |
| $\rho$ | density (kg/m³) |
| $\lambda$ | heat conductivity (W m⁻¹ K⁻¹) |
| $\lambda_p$ | pore diameter (m) |
| $\omega$ | humidity ratio (kg/kg) |
| $v$ | kinematic viscosity (m² s⁻¹) |
| $\delta$ | membrane thickness (m) |
| $\sigma$ | porosity |
| $\eta_{fin}$ | fin efficiency |
| $\Omega$ | fin conductance parameter |

*Superscripts*

| | |
|---|---|
| $*$ | dimensionless |

*Subscripts*

| | |
|---|---|
| a | air |
| c | cross section |
| e | exhaust air, effective |
| f | fresh air, fiber |
| fin | fin |
| fr | fiber |
| i | inlet, inner |
| Lat | moisture, latent |
| m | mean, membrane, mass |
| max | maximum |
| min | minimum |
| o | outlet, outer |
| s | solid |
| sen | sensible |
| t | transfer |
| tot | total |
| v | vapor |
| w | water |

Membrane-based total heat exchanger has become a key equipment for heat and moisture recovery. The concept is shown in Fig. 1. The device is like a parallel-plates air-to-air heat exchanger. However, in place of common metal foils, membranes that are permeable to water vapor, but impermeable to other unwanted gases like $CO_2$, are used as the plates. Therefore both the sensible heat and the latent heat (moisture) can be exchanged between the incoming fresh air and the outgoing exhaust air. Due to the sensible heat and moisture exchange, heat and humidity would be recovered from the exhaust stream in winter (especially in cold climates like in Beijing) and excess heat and moisture would be transferred to the exhaust in order to cool and dehumidify the incoming fresh air in summer. With total heat exchangers, 70–90% of the energy for conditioning fresh air could be saved [7].

Although energy savings potential is great, there are great challenges to fulfill this task. The reasons are: (1) the temperature and humidity differences between the fresh air and the exhaust air are small, around 10 °C and 10 g/kg respectively. A large heat and mass transfer area is required to have an acceptable recovery effectiveness. This leads to challenges in compactness. (2) The initial and

maintenance fee for energy saving equipments should be low enough to attract market attention. This leads to challenges in material selection. In summary, heat and moisture recovery is an
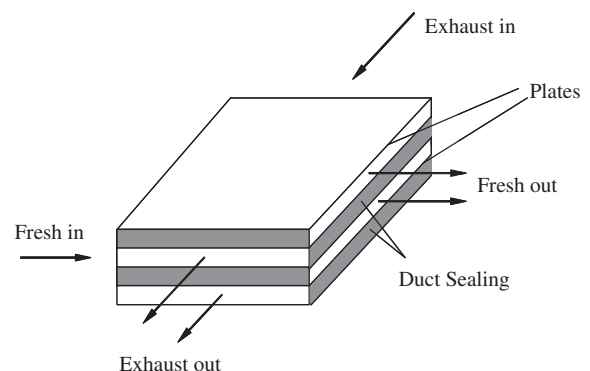


**Fig. 1.** Schematic of a parallel-plates total heat exchanger.

interesting yet challenging task. Over the past 10 years, accommodating the local weather conditions, to satisfy the social and market demands, the center of energy saving technologies for built environment of South China University of Technology has conducted many researches on this topic, from fundamentals to engineering applications. This paper gives a review on the progress of these works. They include: new concepts in heat and moisture transfer, new materials fabrications, new exchanger structure configurations, and pioneering engineering applications. The current status quo will be introduced and future research directions will be pointed out.

## 2. Novel concepts in heat and moisture transfer

### 2.1. Evaluation of moisture diffusivity

Moisture diffusivity in membranes is a key parameter influencing system performance. The traditional way of moisture permeation test did not consider the convective mass transfer resistance on the membrane surface. The measured values are in fact the overall parameters. The measured diffusivity varies with operating conditions like air velocities. To address this problem, our laboratory proposed a new approach [37,38]. The convective mass transfer resistance is separated first and clarified from the overall resistance [39]. The diffusivity in the membrane itself is thus obtained.

An emission cell is designed to measure the moisture diffusivity in membranes. The flow geometry and the membrane in the cell are shown in Fig. 2. It is composed of two parts: cap and lower chamber. In the test, distilled water or saturated salt solution is poured into the lower chamber of the cell. Then a polymer membrane is covered on the lower chamber. Following this step, the cap of the cell is placed on the membrane to form a sandwiched structure. A 2 mm gap between the water layer and the membrane is kept. The upper surface of the membrane and the inner surface of the cap form a cone-shaped cavity. The air is supplied through the air slits in the cap. It is introduced through two diametrically positioned inlets (symmetrically placed) into a circular-shaped channel at the perimeter, from where the air is distributed over the membrane surface through the circular air slit. The air flows radially inward, until it exits the cell outlet in the center. The distilled water or saturated solution in the lower chamber supplies a constant humidity ratio below the membrane lower surface. When the humidity ratio between the two sides of the membrane is different, moisture will diffuse through the membrane. Humid air is supplied from the inlets of the cap, which will exchange moisture with the membrane and the humidity ratio will change along the path. During the test, the temperature is kept constant. The relative

humidity of the inlet and the outlet air streams are measured, and the moisture exchange effectiveness can be calculated.

The complete test rig is shown in Fig. 3. The cell is supplied with clean and humidified air from an auxiliary air supply unit. The supply air flows from a compressed air bottle and is purified through an AC carbon column filter and is then split into two streams. One of them is humidified through a bubbler immersed in a bottle of distilled water, and then re-mixed with the other dry air stream. The outlet humidity from the bottle with bubbler reaches nearly 100%. The humidity of the mixed air stream is controlled by adjusting the ratios of air mixing by two needle valves on each stream. The desired relative humidity is obtained with this method. The airflow rates are controlled by two air pumps/controllers at the inlet and outlet of the cell. To prevent outside air from infiltrating into the cell, a manometer is installed to monitor the pressure inside the cell and ensure that it is positive. The humidities to and from the cell are measured by RH sensors, which are installed after the pumps/controllers.

The overall moisture transfer coefficient is [37]

$$K = \frac{1}{\frac{1}{k} + \frac{2\rho_a z_0}{D_{vm}\rho_m k_p}} \tag{1}$$

where $z_0$ is the distance from water to membrane in the lower chamber (m), $D_{vm}$ is moisture diffusivity in membrane (m$^2$/s), $k_p$ is partition coefficient of membrane material, and the convective mass transfer coefficient $k$ was obtained previously in separate studies [40,41]. The mass transfer Number of transfer units for the system is defined by

$$NTU_{Lat} = \frac{KA_t}{V} \tag{2}$$

where $A_t$ is the transfer area of the membrane surface (m$^2$), $V$ is the volumetric flow rate of air to the cell (m$^3$/s).

Similar to the analysis of a heat exchanger, a moisture exchange effectiveness can be defined as

$$\varepsilon_{Lat} = \frac{\omega_o - \omega_i}{\omega_L - \omega_i} \tag{3}$$

where subscripts o, i, L refer to air outlet, inlet, saturated humidity of liquid water in lower chamber respectively.

The numerical solution of the governing equations for steady-state moisture transfer in the cell gives the following equations between effectiveness and NTU.

$$\varepsilon_{Lat} = -0.0002NTU_{Lat}^4 + 0.0052NTU_{Lat}^3 - 0.0638NTU_{Lat}^2 + 0.3759NTU_{Lat} + 0.015 \tag{4}$$

With the measured moisture exchange effectiveness, the membrane thermophysical properties, and the experimental conditions are known, $NTU_{Lat}$ can be estimated from this equation. Finally, the diffusivity in membrane can be estimated. The benefits with this approach are that it simultaneously considers the cell fluid dynamics, membrane configurations and operating conditions. The measured values are invariant with measuring conditions.

In a summary, the procedures for moisture diffusivity measurements are: (1) measure the moisture exchange effectiveness with the designed cell; (2) calculate $NTU_{Lat}$; (3) calculate $K$; (4) estimate $D_{vm}$, from known $k$ and other thermal physical properties. This basic yet important parameter will be known finally.

### 2.2. Fractal model [42,43]

This work is to build the relations between membrane performance and micro structures. Porous membranes have been used as the support layer for heat and moisture recovery. Gas diffusivity in porous membranes is a key parameter for system design and
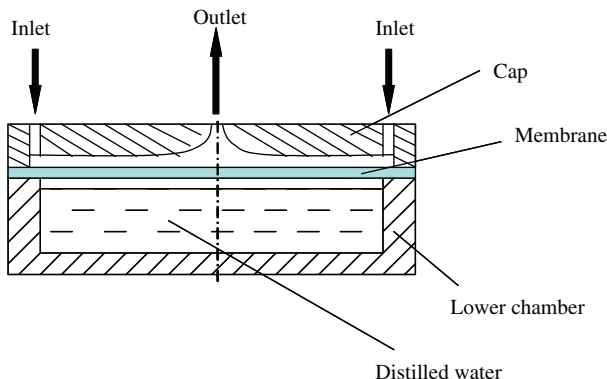


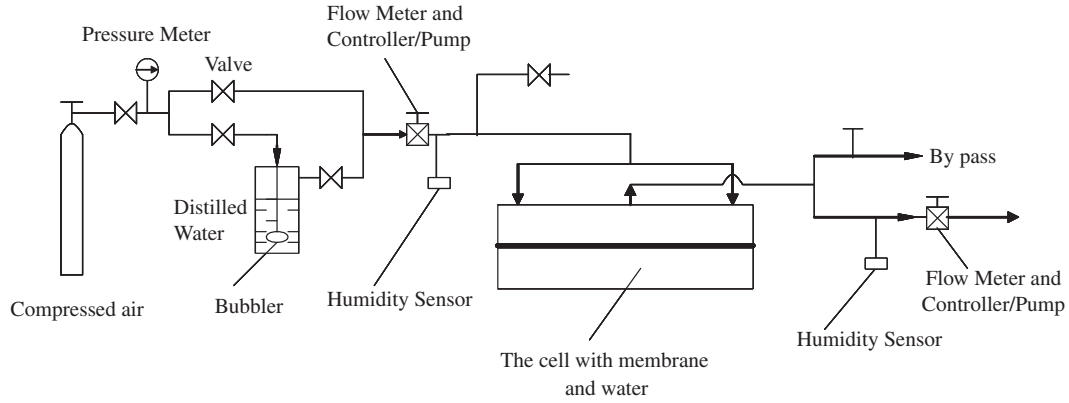**Fig. 2.** A cell to estimate moisture diffusivity through a membrane.

**Fig. 3.** Experimental equipment set-up for moisture transport tests.

membrane optimization [42]. The micro structures of the porous membranes are usually disordered and extremely complicated. This makes it very difficult to analytically find the permeability. In order to get a better understanding of the mechanisms for permeability, a new perspective is considered in the analysis of membrane permeability: fractal models [43].

Fig. 4 shows the SEM (Scanning Electron Micrograph) picture for a typical porous Cellulose Acate membrane. The disordered nature of pore structures in these porous membranes suggests the existence of a fractal structure formed by the macro and micro pores in membranes. These pores and their distributions are analogous in the microstructure to pores in sandstone, to islands or lakes on earth. Therefore, it is possible to obtain the permeability of porous membranes through a fractal analysis on pore microstructures.

Fractal theory is a new theory to analyze natural phenomenon, which allows the characterization of objects in terms of their self-similar (scale invariant) properties (i.e., parts of the object are similar to the whole after rescaling). Fractal techniques have been used in diverse engineering applications that involve physical phenomena in disordered structures and over multiple scales. In all these applications, the fractal dimensions have been very effective in rendering complex structures tractable for analysis, and it is this capability which is explored for describing the membrane structures in the present context.

Porous membrane has numerous pores with various sizes in the through-plane direction, and can be considered as a bundle of tortuous capillary tubes with variable radius for the two-dimensional

case. Let the diameter of a capillary tube be $\lambda_p$, and its tortuous length along the flow direction be $L(\lambda)$. The relationship between them exhibits the fractal scaling law [43]:

$$\frac{L(\lambda_p)}{L_0} = \left(\frac{L_0}{\lambda_p}\right)^{D_t - 1} \tag{5}$$

where $L_0$ is the representative length of a straight capillary, which is equal to membrane thickness. $D_t$ is the tortuosity dimension, with $1 \leqslant D_t \leqslant 2$. Large value of $D_t$ within this range corresponds to a highly tortuous capillary, while $D_t = 1$ denotes a straight capillary pathway, $D_t = 2$, corresponds to a highly tortuous line that fills a plane.

The relationship between the number of pores and the pore size $\lambda_p$ is another important property of fractals. The pores in a porous medium are analogous to the islands or lakes on the earth. The cumulative size distribution of them follows the power law relation [43]:

$$N(L \geqslant \lambda_p) = \left(\frac{\lambda_{p,max}}{\lambda_p}\right)^{D_f} \tag{6}$$

where $N(L \geqslant \lambda_p)$ represents the total number of pores with diameter greater than $\lambda_p$ on unit cell $A_0(= L_0^2)$. $\lambda_{p,max}$ is the maximum pore diameter, $D_f$ is area dimension.

It proves that $\lambda_{p,min} \ll \lambda_{p,max}$ must be satisfied for fractal analysis of a porous membrane. If not, the porous membrane is a non-fractal medium. For those membranes that have relative uniform pore sizes, the fractal theory is not appropriate to use. Fortunately, most porous membranes have wide pore size distributions.

The permeability (m²) through the membrane can be deduced to [43]

$$Pe = \frac{\pi D_f L_0^{1-D_t} \lambda_{p,max}^{D_f}}{128(3 + D_t - D_f)} \left(\lambda_{p,max}^{3-D_f+D_t} - \lambda_{p,K}^{3-D_f+D_t}\right)$$

$$+ \frac{\pi \mu L_0^{1-D_t} D_f \lambda_{p,max}^{D_f}}{12 p_m (2 + D_t - D_f)} \sqrt{\frac{8RT}{\pi M_A}} \left(\lambda_{P,P}^{2-D_f+D_t}\right) \tag{7}$$

where $\lambda_{p,K}$ refers to the pore diameter where gas diffusion changes from Knudsen diffusion to ordinary diffusion, $\lambda_{P,P}$ refers to the pore diameter where viscous Poisseuille flow begins to dominates, $p_m$ is the mean partial pressure of vapor (Pa) in pores, $R$ is ideal gas constant (8.314 J/mol K), $M_A$ is vapor molecule weight (kg/kmol), $\mu$ is the viscosity of vapor (Pa s).

The moisture effective diffusivity $D_e$ (m²/s) through membrane is another important parameter. The relation between diffusivity and permeability is
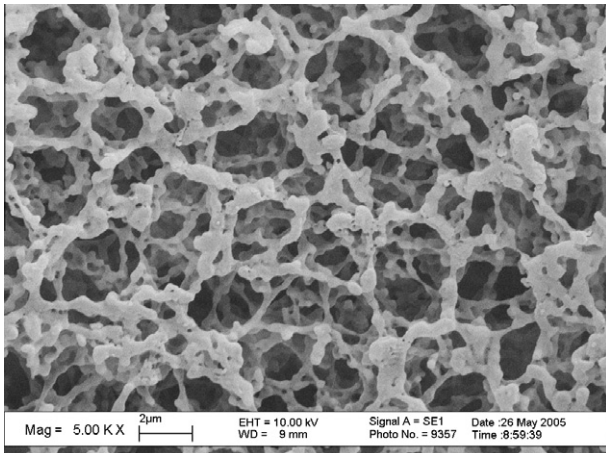


**Fig. 4.** The micro structure of the surface of a Cellulose Acate membrane.

$$D_e = \frac{Pe \cdot RT}{\mu M_A} \tag{8}$$

The area dimension $D_f$ can be determined by the box-counting method. This method is based on the image analysis of a unit cell or a sufficiently large cross section of a sample on the membrane. According to this method, the cross section under consideration is discretized using square boxes of size $L$. Then the number, $N(L \geqslant \lambda_p)$, of boxes required to completely cover the pore areas is countered. The pore area fractal dimension, $D_f$, can be determined by the value of the slope of a linear fit through data on a logarithmic plot of the cumulative number of pores $N(L \geqslant \lambda_p)$ verses the square box size $L$.

The tortuosity dimension $D_t$ represents the extent of convolution of the capillary pathways for gas flowing through the membrane. Since the tortuosity of the flow pathways results from the convolution of the boundaries of the porous regions in membrane cross section, the tortuosity dimension may therefore be evaluated as the fractal dimension of the perimeter of the porous regions on cross section, which may also be obtained by the box-counting method mentioned above.

The maximum pore size in the permeability equation corresponds to the pore space formed between the membrane fibers. The membrane fiber matrix may be considered to be randomly packed ideally equi-spaced aligned fiber screens shown in Fig. 5. For this structure, the maximum pore space may be considered to be resulted from a single ordered membrane fiber screen according to the equation

$$\lambda_{p,max} = 2\sqrt{l_s^2/\pi} \tag{9}$$

where $l_s$ is the length of the representing space.

The above procedures provide the basic data for fractal models. With Eq. (7), the relations between the membrane structure and membrane permeability can be set up. Membrane porosity, mean pore diameter, tortuosity, thickness are the determining factors influencing membrane moisture diffusion. The model provides a new tool for membrane structure optimization.

### 2.3. Effectiveness correlations for performance estimation [44]

Stationary total heat exchangers are similar to air-to-air sensible heat exchangers, either plate type or plate-fin type. The difference is that water vapor-permeable materials are used instead of metal foils. For common heat exchangers, $\varepsilon$–$NTU$ (effectiveness–$NTU$) method is a simple way to predict performance and to design



**Fig. 5.** An ideal membrane fiber matrix.

a heat exchanger. To emulate this methodology to total heat exchanger, $\varepsilon$–$NTU$ correlations are proposed for total heat exchangers.

The definition for sensible and latent effectiveness

$$\varepsilon_{sen} = \frac{(\dot{m}c_p)_f(T_{fi} - T_{fo})}{(\dot{m}c_p)_{min}(T_{fi} - T_{ei})} \tag{10}$$

Latent effectiveness

$$\varepsilon_{Lat} = \frac{(\dot{m}c_p)_f(\omega_{fi} - \omega_{fo})}{(\dot{m}c_p)_{min}(\omega_{fi} - \omega_{ei})} \tag{11}$$

An overall number of transfer units is used to reflect the sensible heat transfer in an sensible exchanger. For the total heat exchanger that has equal area on both sides, the total number of transfer units for sensible heat is

$$NTU_{sen} = \frac{A_{tot}U}{(\dot{m}c_p)_{min}} \tag{12}$$

where $U$ is the total heat transfer coefficient (kW m$^{-2}$ K$^{-1}$). Its general form is

$$U = \left[\frac{1}{h_f} + \frac{\delta}{\lambda} + \frac{1}{h_e}\right]^{-1} \tag{13}$$

The term in the middle is the thermal resistance of plate, which value is around 0.005 m$^2$K/kW. Other two terms are convective thermal resistance. Their values are in the order of 40 m$^2$K/kW, or 8000 times larger than plate resistance. Therefore, plate resistance for heat transfer can be neglected.

The sensible effectiveness is a function of two dimensionless parameters, $NTU$ and $R_1$, the ratio of minimum to maximum heat capacity rate of two air streams.

$$R_1 = (\dot{m}c_{pa})_{min}/(\dot{m}c_{pa})_{max} \tag{14}$$

Similar to the definition of total number of transfer units for heat, the total number of transfer units for moisture can be written as

$$NTU_{Lat} = \frac{\rho_a A_{tot} K}{(\dot{m})_{min}} \tag{15}$$

Similarly, the overall moisture transfer coefficient is defined by

$$K = \left(\frac{1}{k_f} + r_m + \frac{1}{k_e}\right)^{-1} \tag{16}$$

where in the equation, the first and the third term are the convective mass transfer resistance in air sides, and the middle term is membrane mass transfer resistance.

The resistance of membrane in [39] is

$$r_m = \frac{\rho_a \delta}{\rho_m D_{wm}} \psi \tag{17}$$

$$\psi = \left. \frac{10^6 (1 - C_1 + C_1/\phi)^2 \phi^2}{e^{(5294/T)} w_{max} C_1} \right|_{mf} \tag{18}$$

where $\phi$ is relative humidity, $C_1$ is the constant in sorption curve, $w_{max}$ is the maximum water uptake in membrane materials, and $\psi$ is the coefficient of diffusive resistance for plate, which is co-determined by the operating conditions and the slope of sorption curves of plate material.

Following empirical equations are proposed to represent the sensible and latent effectiveness for cross flow total heat exchanger as

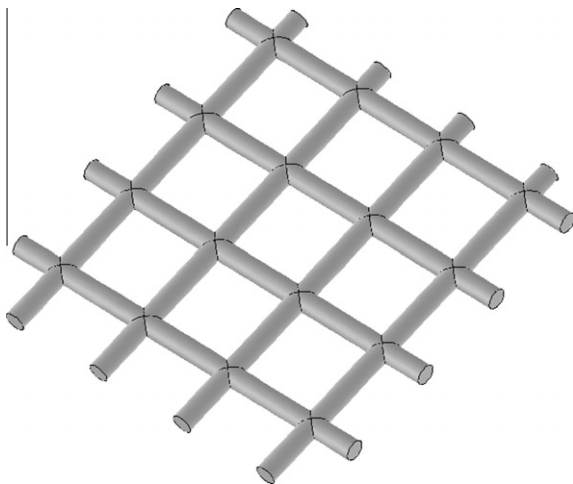$$\varepsilon_{sen} = 1 - \exp\left[\frac{\exp(-R_1 NTU_{sen}^{0.78}) - 1}{R_1 NTU_{sen}^{-0.22}}\right] \tag{19}$$

$$\varepsilon_{Lat} = 1 - \exp\left[\frac{\exp(-NTU_{Lat}^{0.78}R_2) - 1}{NTU_{Lat}^{-0.22}R_2}\right] \quad (20)$$

$$R_2 = \dot{m}_{min}/\dot{m}_{max} \quad (21)$$

We can see at this step that the moisture effectiveness has the same form of expression with sensible effectiveness. The only differences are that $NTU_{sen}$ is replaced by $NTU_{Lat}$ and $R_1$ is replaced by $R_2$.

The latent effectiveness correlations for other flow arrangements, such as concurrent flow and counter flow, can also be derived from those corresponding correlations for sensible effectiveness, using the definition of Eqs. (10)–(18).

For concurrent flow,

$$\varepsilon_{Lat} = \frac{1 - \exp[-NTU_{Lat}(1 + R_2)]}{1 + R_2} \quad (22)$$

For counter flow,

$$\varepsilon_{Lat} = \frac{1 - \exp[-NTU_{Lat}(1 - R_2)]}{1 - R_2\exp[-NTU_{Lat}(1 - R_2)]} \quad (R_2 < 1) \quad (23)$$

$$\varepsilon_{Lat} = \frac{NTU_{Lat}}{1 + NTU_{Lat}} \quad (R_2 = 1) \quad (24)$$

The sensible effectiveness can also be calculated with above equation if $NTU_{Lat}$ is replaced by $NTU_{sen}$ for each flow arrangement.

### 2.4. Facilities for heat and moisture exchange through membranes

#### 2.4.1. Single membrane [45]

An experimental set up has been built to study the simultaneous heat and moisture transport through a single membrane. The whole test rig is shown in Fig. 6. Ambient air is humidified and is driven to a heating/cooling coil in a hot/cool water bath. The cooling coil can also act as dehumidifier when necessary. After the temperature and humidity reach test conditions, the air is then sucked through the exchanger for heat and moisture exchange. This flow is denoted as the hot and humid fresh stream. Another flow is driven directly from indoor to the exchanger. It is denoted as the cool and dry exhaust flow. The membrane, which is developed in the laboratory, is sandwiched by two stainless steel rectangular shells. Two parallel rectangular air passages on both sides of membrane are formed, which is like a one-plate plate-and-shell heat exchanger. In the test, a 10 mm thick insulation layer is placed on the inner surface of the shell to prevent heat dissipation from the shell to the surroundings. Moisture dissipation from air stream to the surroundings is negligible. After the exchanger and pipes are installed, additional insulation is added on the outside surfaces to minimize heat losses from the unit.

The nominal operating conditions: fresh air inlet 35 °C and 0.021 kg/kg; exhaust air inlet 25 °C and 0.010 kg/kg. The corresponding inlet relative humidity (RH) is 59% and 51% for fresh air and exhaust air respectively. During the experiment, air flow rate is changed by variable frequency pumps, to have different air velocities. Humidity, temperature, and volumetric flow rates are monitored at the inlet and outlet of the exchanger. To have a balanced flow, equal air flow rates are kept for the two air streams. Typical air velocities are from 0.5 m/s to 3 m/s which are typical for commercial total heat exchangers. Air flow under such conditions is laminar, with Reynolds numbers not exceeding 500. The uncertainties are: temperature ±0.1 °C; humidity ±2%; volumetric flow rate ±1%. The final uncertainty for effectiveness and heat transfer coefficients is ±4.5%.

After the measurement of inlet and outlet temperature and humidity, the sensible effectiveness and the latent effectiveness can be calculated by Eqs. (10) and (11). Further, the overall mass transfer coefficient through the membrane can be calculated by

$$K = \frac{u_a A_c(\omega_{fi} - \omega_{fo})}{A_t \Delta\omega_{lm}} \quad (25)$$

where $u_a$ is air velocity (m/s), $A_c$ is the cross section area of air duct (m²), $A_t$ is the transfer area of membrane in the cell (m²), $\Delta\omega_{lm}$ is the logarithmic mean humidity difference between the two air streams. For counter flow, it is calculated by

$$\Delta\omega_{lm} = \frac{(\omega_{fi} - \omega_{eo}) - (\omega_{fo} - \omega_{ei})}{\ln\frac{(\omega_{fi} - \omega_{eo})}{(\omega_{fo} - \omega_{ei})}} \quad (26)$$

Besides overall mass transfer coefficient, permeability coefficient, Pe′ (g/(cm² s cm Hg)) is another parameter to reflect moisture permeability through membranes, if the membranes have similar thickness. The relation between $k$ and Pe′ is

$$Pe' = K/1040 \quad (27)$$

#### 2.4.2. Real exchanger element [46]

An application scale total heat exchanger element usually comprises of a stack of 200–300 membranes, as shown in Fig. 7. A test-rig has been built to measure the sensible and latent effectiveness of an application scale element, as shown in Fig. 8. Volumetric air flow rates are from 100 to 700 m³/h. The real equipments are shown in Fig. 9. The control system of the room is not plotted because of camera reasons. Two parallel air ducts with a 200 × 200 mm cross section are assembled. Each duct is comprised of a variable speed blower, a wind tunnel, a set of nozzles, wind straighteners, electric heating coils, steam humidification tubes, temperature and humidity sensors. An exchanger shell is designed to hold the core. The small converging wind tunnels produce steady, homogeneous, fully developed air flow to the exchanger. The
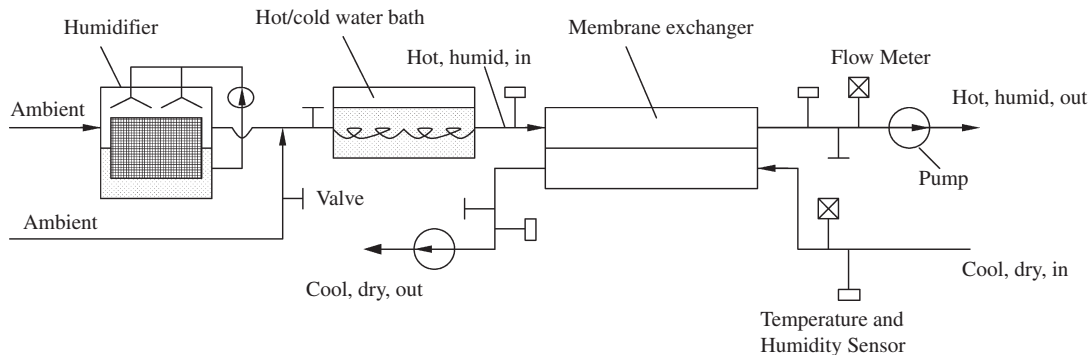


**Fig. 6.** Schematic of the heat and moisture transfer test rig for a single membrane.
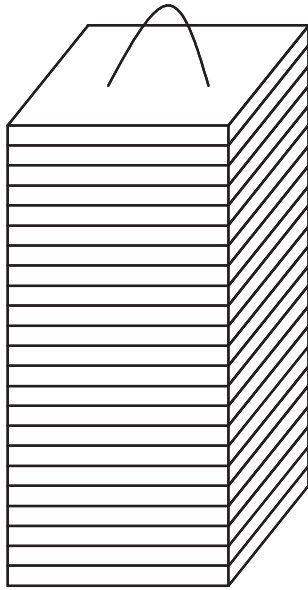
**Fig. 7.** A real total heat exchanger element.



**Fig. 9.** A picture showing the real test rig for element.

## 3. Novel membranes

### 3.1. Hydrophobic–hydrophilic composite membrane

Membrane materials are the key components for heat and moisture recovery technology. Hydrophilic polymer membranes that are permeable to vapor, but impermeable to air, have been considered for moisture permeation. Traditionally they are homogeneous membranes. Typical materials include [7,47]: Nafion, regenerated cellulose, cellulose triacetate, sulfonated poly(phenylene oxide), polyether-polyurethane, siloxane-amido copolymer, polystyrene-sulfonate, polyvinylidene fluoride and polyethersulfone, and cellophane. These materials are reasonable choices since they have already been used in air dehumidification applications which have similar moisture transfer mechanisms to moisture recovery. However, moisture diffusion coefficients in such polymer membranes are usually very low, in the order of $10^{-12}$–$10^{-13}$ m$^2$/s, while total heat exchangers only have limited transmembrane vapor partial pressure difference, consequently performances are quite limited with them.

heating power and the steam generation currents can be adjusted according to the set points temperature and humidity. After the air temperature and humidity are adjusted to the set points, the two ducts are connected to the two inlets of the exchanger shell respectively. The exchanger shell is designed to station the exchanger element and separate the cross flow two air streams. The element can be inserted into the quadrate cavity in the center of the shell. The whole test rig is built in a constant temperature and constant humidity room, so the inlet temperature and humidity can be controlled and maintained very well even under very hot and humid ambient weather conditions. The heat loss from the system is below 0.5%, and moisture loss is less than 0.1%. Humidity, temperature, and volumetric flow rates are monitored at the inlet and outlet of the exchanger. Then the sensible and latent effectiveness are calculated.
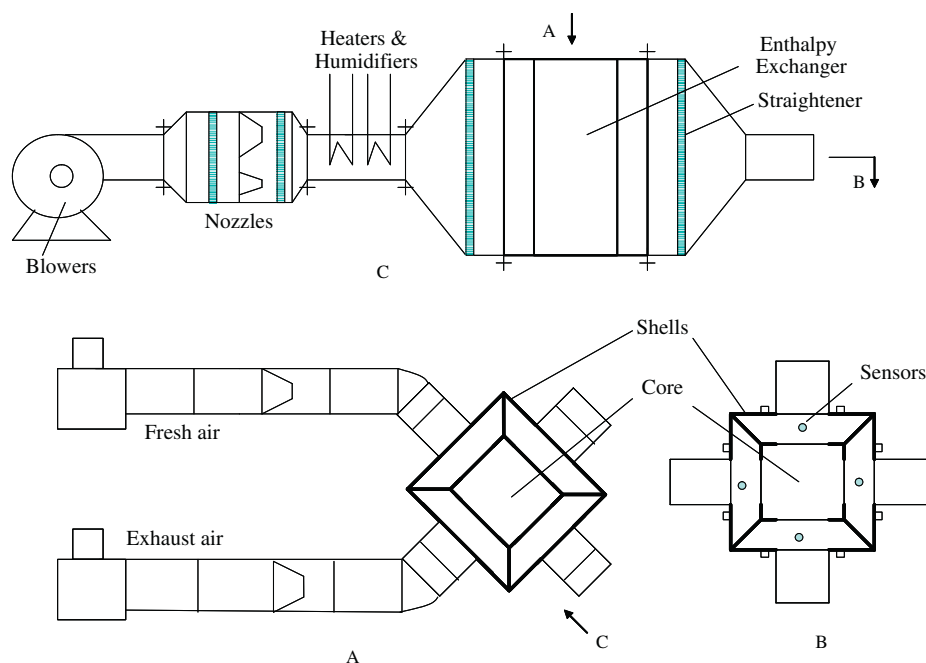


**Fig. 8.** Experimental set-up of the real total heat exchanger element.

To address this problem, in our laboratory, several novel membranes are made. They are: hydrophobic–hydrophilic composite membranes [47,48], composite supported liquid membranes [49–52], and membranes with finger-like macrovoids [53].

Vapor diffusion in homogeneous membranes is rather small. To increase vapor permeation rates, a hydrophobic–hydrophilic dual polar composite membrane have been made. According to this scheme, a thin active layer is cast onto a thick porous PP (polypropylene) support layer or other materials. The porous support layer provided the necessary mechanical strength while the thin active layer provided the permselective separating effect. The permeation rates can be greatly improved due to the reduction in resistance. The structure is depicted in Fig. 10.

### 3.1.1. Membrane preparation

The composite membrane is formed by coating CTA casting solution onto the PP support membrane. The fabrication process is comprised of the following three steps [47,48]:

(1) Formulation of casting solution. CTA powder is weighted and placed into a vessel with Acetone at about 90 °C. The solution is heated and stirred until it is completely dissolved. It took about 2 h.

(2) A certain amount of cross-linking agent (e.g. L-malic acid), catalyst (e.g. glacial acetic acid) and additive (LiCl) is added to the solution. The solution is continuously stirred at 70 °C until these different compositions are completely dissolved to form a homogeneous solution. The solution is cool down and placed still for de-bubbling. It took 2 h.

The polymer solution is coated on the PP support membrane. The thickness of the active layer is controlled by a casting knife. The thickness of the final active layer can be from several microns to a dozen microns, depending on the gap between the knife edge and the support layer. Then the asymmetric membrane is placed into a vacuum drying oven for cross-linking at 100 °C for 1 h. The membrane is further dried at 60 °C for 2 h.

### 3.1.2. Heat and moisture transfer in the membrane

The membrane is composed of two layers. The heat and moisture transfer through the membrane can be depicted by a model shown in Fig. 11.

Moisture flux through the composite membrane is expressed by

$$J = \rho_a D_e \frac{\omega_1 - \omega_2}{\delta_1 + \delta_2} \tag{28}$$

where $D_e$ is the effective moisture diffusivity in the composite membrane (m²/s), it is calculated by

$$D_e = \frac{\delta_1 + \delta_2}{\frac{\delta_1}{D_{e1}} + \frac{\delta_2}{D_{e2}}} \tag{29}$$

where $D_{e1}$, $D_{e2}$ are the effective diffusivity in the first layer and second layer, respectively.

The effective diffusivity can be calculated according to their diffusion mechanisms. The established theory of gas diffusion in hydrophobic membranes considers three mechanisms: Poiseuille flow, ordinary molecular diffusion and Knudsen diffusion, or a



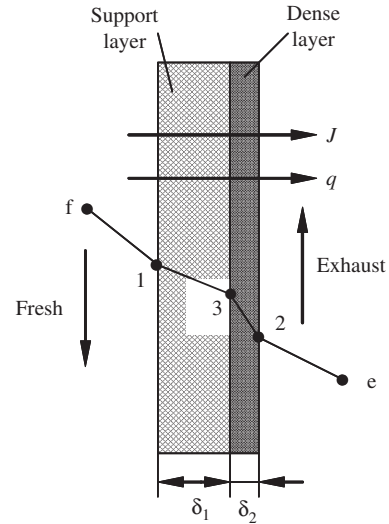Fig. 10. Composite hydrophobic–hydrophilic membrane structure.



Fig. 11. Transfer model through the composite membrane.

combination of them. In the support layer, $D_{e1}$ can be calculated as the combined Knudesn and ordinary diffusion [48], taking into account of porosity and tortuosity.

Rather than by gas diffusion as in hydrophobic layer, it is believed that moisture transfer in the second layer is as following: the water vapor is first adsorbed to the membrane surface adjacent to support layer, then it diffuses to the exhaust air side in water state, and at last it is desorbed from the surface of hydrophilic layer adjacent to exhaust air.

$$D_{e2} = \frac{\rho_2 k_p D_{w2}}{\rho_a} \tag{30}$$

$D_{w2}$ is water diffusivity in the second layer (m²/s), $\rho_2$ is density of this layer (kg/m³), $k_p$ is the partition coefficient, which reflects the sorption properties of moisture in membranes.

Heat flux through the composite membrane

$$q = \frac{\lambda_e(T_1 - T_2)}{\delta_1 + \delta_2} \tag{31}$$

$$\lambda_e = \frac{\delta_1 + \delta_2}{\frac{\delta_1}{\lambda_1} + \frac{\delta_2}{\lambda_2}} \tag{32}$$

The heat conductivity in porous media is [43,53]

$$\lambda_1 = (\lambda_a^{1/4}\sigma + \lambda_s^{1/4}(1-\sigma))^4 \tag{33}$$

where subscripts a and s denote moist air and solid material part, respectively; $\sigma$ is porosity of membrane. The estimation method of heat conductivity for layer 2 is the same as layer 1.

### 3.2. Composite supported liquid membrane [49–52]

Moisture diffusivity in solid polymer membranes is usually very low, in the order of $10^{-12}$–$10^{-13}$ m²/s. In contrast, moisture diffusivity in liquid is several orders higher than in solid membranes. A new membrane has been proposed in our laboratory to enhance moisture transfer: the composite supported liquid membrane.

The concept is schematically depicted in Fig. 12. It employs LiCl liquid solution immobilized in a porous support membrane to facilitate the transport of moisture. To protect the SLM, two hydrophobic PVDF (polyvinylidene fluoride) layers are formed on both surfaces of the SLM. The sweep represents exhaust air.
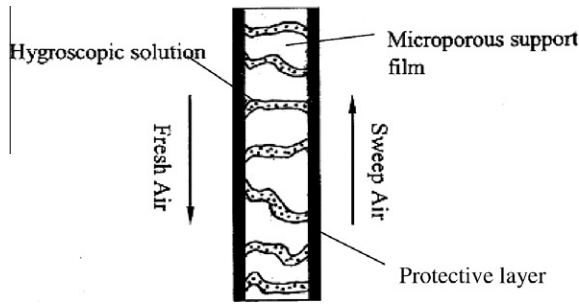
**Fig. 12.** Concept of the composite supported liquid membrane (CSLM).

### 3.2.1. Preparation of the membrane

Under room temperature, well-stirred LiCl solution with 40% mass fraction is first prepared in a closed glass container. Vacuum degassing is applied for 2 h for the three membranes, after which, a CA membrane is dipped into the LiCl solution. After 24 h, the CA membrane is moved from the solution and placed onto a clean glass plate which is cleaned by alcohol. Surplus LiCl solution on surfaces of CA membrane is blotted off with paper tissue. To be sure that no ionic liquid is removed from the membrane pores, the cleaning procedure is very gentle. At this stage, PVC glue is brushed on one surface of the two PES membranes, and at the same time on both surfaces of the CA membrane. After a few seconds, the two PES membranes are glued to the CA membrane and are pressed together gently for a few seconds. The prepared composite membrane is placed in a constant-temperature–constant-humidity chamber for another 24 h, before experiment is performed.

### 3.2.2. Heat and moisture transfer in the membrane

Heat and moisture transfer through the membrane can be depicted by a model shown in Fig. 13.

Moisture flux through the composite membrane is expressed by

$$J = \rho_a D_e \frac{\omega_1 - \omega_4}{\delta_1 + \delta_2 + \delta_3} \tag{34}$$

where $D_e$ is the effective moisture diffusivity in the composite membrane (m$^2$/s), it is calculated by

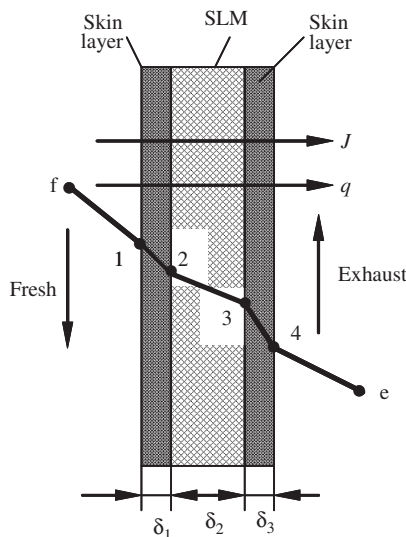$$D_e = \frac{\delta_1 + \delta_2 + \delta_3}{\frac{\delta_1}{D_{e1}} + \frac{\delta_2}{D_{e2}} + \frac{\delta_3}{D_{e3}}} \tag{35}$$

where $D_{e1}$, $D_{e2}$, $D_{e3}$ are the effective diffusivity in the first, second, and third layer, respectively.

The estimation of moisture diffusivity in the first and the third layers are the same as the first layer in above section for composite solid membrane. The equivalent diffusion coefficient of vapor in liquid membrane is

$$D_{e2} = \frac{1.608 P_a k_p \sigma_2}{\rho_a \tau_2} D_{wl} \tag{36}$$

where $D_{wl}$ is water diffusivity in liquid solution (m$^2$/s), $P_a$ is air pressure, $\tau_2$ is tortuosity of layer 2, $k_p$ is partition coefficient of this layer. Water vapor partial pressure, temperature, and LiCl solution concentrations are strongly coupled and governed by thermodynamic equations [49].

The heat conductivity in the first and third layer can be analyzed based on Eq. (33). The heat conductivity in the second layer, where a liquid solution is stationed in the porous media, can be analyzed by

$$\lambda_2 = \lambda_{lq}\sigma_2 + \lambda_s(1 - \sigma_2) \tag{37}$$

where subscripts lq denote liquid solution.

### 3.3. Membranes with finger-like macrovoids [53]

Phase-inversion method has been the widely used technology for membrane preparation since it was successfully used by Loeb and Sourirajan to develop cellulose acetate membranes for seawater desalination in 1960s [7]. According to this method, the formation of membrane structure is controlled by both the thermodynamics of the casting solution and the kinetics of transport process. Usually, depending on the rate of phase separation, two different structures, namely a symmetric sponge-like (from delayed phase demixing) or an asymmetric finger-like structure (from instantaneous phase demixing) can be expected. Fig. 14 shows a typical asymmetric finger-like structure. It is composed of three parts from bottom to top: a sponge-like porous support, a porous media with finger-like and nearly parallel macrovoids, and finally a very thin skin layer with rather small pores. Due to the existence of large finger-like macrovoids, it is qualitatively believed that the asymmetric membranes have less resistance than symmetric membranes, and thus are beneficial for permeation performance.
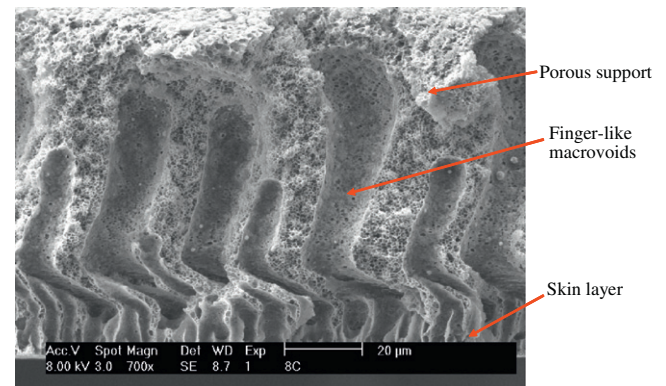


**Fig. 13.** Heat and mass transfer model in the composite supported liquid membrane.



**Fig. 14.** SEM graph of the cross section of an asymmetric porous membrane.

### 3.3.1. Preparation of the membrane

Industrial grade PVDF (polyvinylidene fluoride) is used as the membrane raw material. The membrane is fabricated through following steps: (1) 15 g PVDF powder is weighted and placed into a vessel with 100 g DMF (N,N-dimethylformamide) at about 90 °C. The solution is heated and stirred until it is completely dissolved. It takes about 2 h. (2) 3 g PEG (polyethylene glycol) and PVP (polyvinyl pyrrolidone) is added to the solution and kept stirring for another 2 h. (3) The solution is degassed and cast onto a clean glass plate with appropriate thickness control by a knife edge. (4) The glass with cast solution is dipped into a 25 °C water bath. Immediately, the solution solidifies and peels off the glass plate to form a membrane sheet. The membrane is soaked in water bath for 24 h for solvent and non-solvent exchange. (5) The membrane is dried in a vacuum drying box for 10 h. (6) The membrane is ready for structural characterization.

The membrane structure is schematically depicted in Fig. 15. It is composed of three layers: a sponge-like porous layer, a sponge layer with finger-like macrovoids, and a skin layer. Their dimensions are plotted in the figure. Though the macrovoids may have differences, more or less, in length and dimension, in the model, they are approximated as identical cylinders, to ease the mathematical analysis. To account for their zigzag nature, a tortuosity is used to compensate this feature.

### 3.3.2. Heat and moisture transfer in the membrane

Generally, resistance model is convenient in calculating heat mass transfer through a multi-component media. Gas diffusion through the asymmetric membrane can be depicted by the
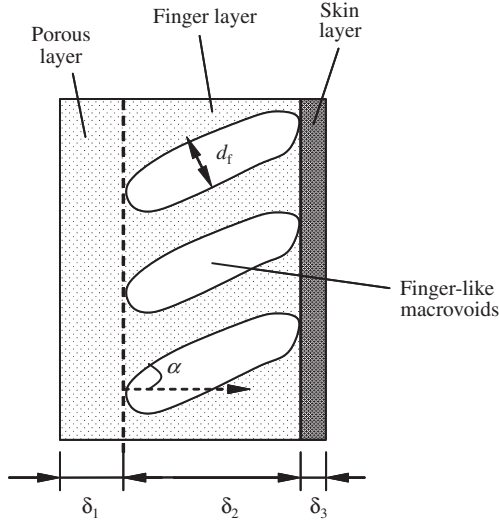


**Fig. 15.** Simplified structure of a finger-like macrovoids asymmetric membrane.

resistance model as shown in Fig. 16. The mechanism for gas diffusion is combined Knudsen and ordinary diffusion.

The gas diffusion resistance in the first layer is (s/m)

$$r_1 = \frac{\delta_1}{D_{e1}} \tag{38}$$

The resistance through the second layer comprises of two parallel parts: the finger-like macrovoids and the sponge-like micro pores. The resistance through the finger-like macrovoids

$$r_{2f} = \frac{\tau_{2f} l_f}{\sigma_{2f} D_{2f}} \tag{39}$$

where $\tau_{2f}$ is the tortuosity of finger-like macrovoids in the second layer. For straight capillaries, tortuosity value is 1.0, for rather zigzag channels, tortuosity is always given a value of 3.0. In the equation, $l_f$ is the length of macrovoids. $D_{2f}$ is Gas diffusivity through macrovoids by substituting macrovoid mean diameter as the character pore size.

Besides gas diffusion through macrovoids, there is still some diffusion through the residual sponge like micro pores in this layer. The resistance through this part is

$$r_{2s} = \frac{\tau_1 \delta_2}{\sigma_1 (1 - \sigma_{2f}) D_1} \tag{40}$$

where in the equation, the tortuosity, porosity, and diffusivity are considered as the same as the first layer, since they are similar in structure from SEM observations. The finger-like macrovoids walls has the same structure as the porous substrate. The calculation of diffusivity in the third layer is the same as in the first layer.

According to Fig. 16, the total resistance for membrane

$$r_{tot} = r_1 + (r_{2f}^{-1} + r_{2s}^{-1})^{-1} + r_3 \tag{41}$$

Effective mass diffusivity through the whole membrane

$$D_e = \frac{\delta_1 + \delta_2 + \delta_3}{r_{tot}} \tag{42}$$

Heat conductivity in the first layer and third layer can be calculated by Eq. (33). In the second layer, considering the media having a porosity of $\sigma_{2f}$, and a solid part heat conductivity of $\lambda_1$, a form similar to Eq. (33) can be used

$$\lambda_2 = \lambda_a \sigma_{2f} + \lambda_1 (1 - \sigma_{2f}) \tag{43}$$

Overall effective thermal conductivity

$$\lambda_e = \frac{\delta_1 + \delta_2 + \delta_3}{\delta_1/\lambda_1 + \delta_2/\lambda_2 + \delta_3/\lambda_3} \tag{44}$$

It should be noted that membrane thermal resistance is rather smaller than boundary resistance on membrane two surfaces, due to the small thickness of membranes.

Resistance in the membrane is analyzed. It is found that the second layer has the highest gas diffusivity through a single pore or finger. This is because that the larger the pore (finger) diameter,
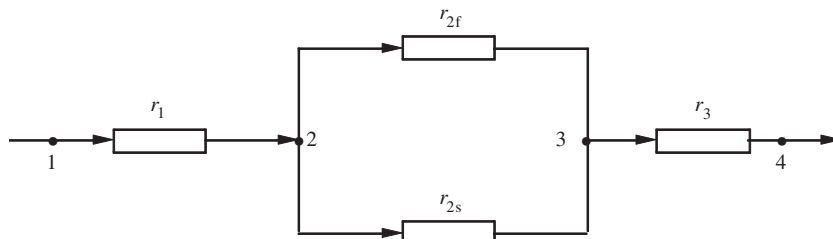


**Fig. 16.** Resistance model in the asymmetric membrane.

the higher the gas diffusivity. Nevertheless, the diffusivity through a finger ($D_{2f}$) is in the same order with the diffusivity through a small pore ($D_3$). Due to the existence of straight finger voids, the total porosity in the second layer is greatly improved, and consequently the effective gas diffusivity through this layer ($D_{2e}$) is one order higher than that through the sponge support layer ($D_{1e}$). In one word, due to the increased porosity by straight finger voids, effective diffusivity can be greatly improved.

## 4. Novel structures for total heat exchanger

### 4.1. Parallel-plates [45,54]

#### 4.1.1. Configurations

Parallel-plates channels are the most simple and common structures for heat and moisture recovery. The structure has been shown in Fig. 1. Heat transfer in this structure has been well introduced in classical textbooks. However in membrane-formed parallel-plates channels, the phenomenon becomes more complex. Two difficulties should be overcome: (1) the boundary values are neither uniform temperature nor uniform heat flux on membrane surface. It is a conjugate problem in nature. In addition, besides heat transfer, there is simultaneous mass transfer. (2) A large proportion of the channel length is in entry regions. Since the Nusselt and Sherwood numbers in the entry regions are higher than in developed regions, a fully developed flow assumption would lead to substantial underestimations.

In our study, heat and mass transfer in the two air streams and in the membrane are considered as two conjugate problems. The conjugate heat transfer problem is first solved with a CFD code, which is convenient and efficient in solving conjugate heat transfer problems. The conjugate mass transfer problem is solved by first transferring it to another conjugate heat transfer problem by heat mass analogy. The solution of these two conjugate problems gives the temperature and humidity distributions in the air streams and on membrane surfaces, and consequently the Nusselt and Sherwood numbers.

#### 4.1.2. Convective heat and mass transfer in ducts

The hydrodynamic and heat and mass transfer problem can be described by Navier–Stokes equations as shown in [54]. Heat and mass transfer in ducts should be coupled with heat and mass transfer in membranes. At the positions where fluid contacts with membrane (on two surfaces), velocity is set to zero (no-slip boundary condition). Temperature and humidity in fluid and on membrane surface are coupled by heat mass flux expressions as following.

$$q = -\lambda_a \frac{\partial T}{\partial z}\bigg|_{surface} = -\lambda_m \frac{\partial T}{\partial z}\bigg|_{surface} \tag{45}$$

$$J = -\rho_a D_{va} \frac{\partial \omega}{\partial z}\bigg|_{surface} = -\rho_m D_{vm} \frac{\partial \omega}{\partial z}\bigg|_{surface} \tag{46}$$

where $z$ is in membrane thickness direction. With these equations, the properties in the fluid are connected with those in membranes.

Convective mass transfer coefficient $k$ (m/s) and heat transfer coefficient $h$ (kW m$^{-2}$ K$^{-1}$) in ducts can be represented by Sherwood and Nusselt numbers respectively as

$$Sh = \frac{kd_h}{D_{va}} \tag{47}$$

$$Nu = \frac{hd_h}{\lambda} \tag{48}$$

Other definitions significant for transport are

$$Le = \frac{Pr}{Sc} \tag{49}$$

$$Pr = \frac{v}{\alpha} \tag{50}$$

$$Sc = \frac{v}{D_{va}} \tag{51}$$

where $D_{va}$ represents moisture diffusivity in air; $Le$ is the Lewis number of air; Pr and Sc are Prandtl number and Schmidt number respectively, $v$ and $\alpha$ are kinematic viscosity and thermal diffusivity for air, respectively (m$^2$/s).

After the solution of conjugate heat and mass transfer equations in the membrane-formed ducts, the Nusselt and Sherwood numbers are obtained. The results show that the local friction factor, the Nusselt number and the Sherwood number are very large at the air inlets. They decrease steadily and reach stable values after the boundaries are fully developed. The membrane to fluid diffusivity ratios have great influences on the fully developed Nu and Sh numbers.

Table 1 lists the calculated fully developed Nusselt numbers and Sherwood numbers for three flow arrangements with various membrane conductivity or diffusivity ratios. Membrane heat conductivity ratio less than 1.0 or membrane diffusivity ratios greater than 0.3 only have numerical meanings. They are used just to disclose the effects of various membrane resistance on fluid heat mass transfer numerically.

As seen from Table 1, the effects of membrane resistance on fully developed Nusselt and Sherwood numbers in fluids are negligible. The Sherwood numbers are usually less than Nusselt numbers, due to the different values of Pr and Sc. Generally, flow arrangements and membrane resistance have some degree of influences on Nusselt or Sherwood numbers, however they are very small. The counter flow arrangement has the largest Nusselt and Sherwood numbers. The cocurrent flow has the lowest values. The fully developed Nusselt number under uniform temperature condition is $Nu_T = 7.54$, and that under uniform heat flux condition is $Nu_H = 8.23$. As indicated, the Nusselt numbers under counter flow are close to $Nu_H$, and those under cocurrent flow are close to $Nu_T$. The values under cross flow are in the middle.

The boundary conditions on membrane surfaces are the results of coupling between the two neighboring fluids. Membrane to fluid heat conductivity ratio and membrane to fluid diffusivity ratio play leading roles in affecting the temperature and humidity distributions in fluids and in membrane. Different ratios would have different temperature or humidity values on membrane surfaces, thus changing the boundary conditions.

### 4.2. Plate-fin ducts [55–60]

#### 4.2.1. Configurations

Plate-fin ducts are the common structure for compact heat exchanger design. The structure is shown in Fig. 17. It is mechanically

**Table 1**
Fully developed Nusselt, Sherwood numbers for parallel-plates channels with different membrane to fluid conductivity ratios ($\tau_0$), under three typical arrangements.

| $\tau_0$ | Cocurrent flow | | Cross flow | | Cross flow | |
|---|---|---|---|---|---|---|
| | Nu | Sh | Nu | Sh | Nu | Sh |
| 0.1 | 8.01 | 7.03 | 8.17 | 7.22 | 8.12 | 7.13 |
| 1 | 8.04 | 7.05 | 8.19 | 7.51 | 8.14 | 7.23 |
| 10 | 8.06 | 7.06 | 8.21 | 7.33 | 8.16 | 7.26 |

*Notes*: $\tau_0$, Membrane to fluid conductivity ratios. For fully developed flow under uniform temperature, $Nu_T = 7.54$; for fully developed flow under uniform heat flux condition, $Nu_H = 8.23$.
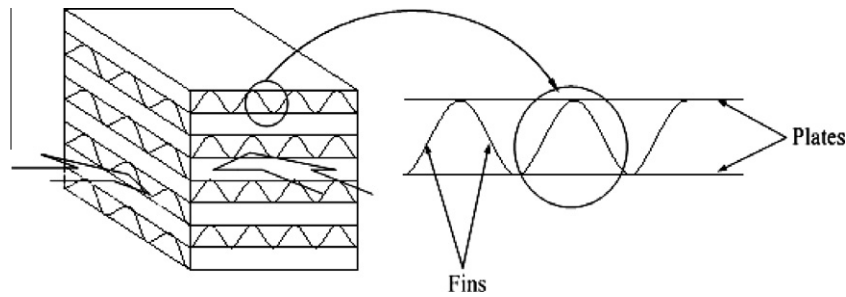
**Fig. 17.** Schematic of a plate-fin structure.

strong, compact, and high efficient. Ducts of well-conductive materials and with regular cross sections have been studied in classical textbooks. Ducts of common well conductive materials but with irregular cross sections are modeled with boundary fitted coordinates [55,56]. Recently, our laboratory has extended the studies with boundary fitted coordinates to plate fin ducts of non-metal materials which have lower fin heat and mass conductance parameters [57–60].

### 4.2.2. Convective heat and mass transfer in ducts

At any location along the fin, there is a balance between the net conduction along the fin and the heat transfer from the surface of the fin to the fluid. The heat flux at the lower surface and the upper surface are skew symmetric [57]. The one dimensional heat and mass transfer equations in ducts are solved in combination with the solution of heat and mass transfer equations in fins.

Fin heat conductance parameter is defined by

$$\Omega_{\text{sen}} = \frac{\lambda_{\text{fin}}\delta}{\lambda_{\text{a}}(2a)} \qquad (52)$$

Fin mass conductance parameter is defined as

$$\Omega_{\text{Lat}} = \frac{\delta\rho_{\text{fin}}D_{\text{w,fin}}k_{\text{p}}}{\rho_{\text{a}}D_{\text{va}}(2a)} \qquad (53)$$

where $a$ is half the channel pitch (or half fin height).

Fin efficiency for heat transfer is defined as the ratio of Nu at a finite fin heat conductance to that at $\Omega_{\text{sen}} = \infty$, or

$$\eta_{\text{fin}} = \frac{\text{Nu}_{\Omega_{\text{sen}}}}{\text{Nu}_{\Omega_{\text{sen}}=\infty}} \qquad (54)$$

Fin efficiency for mass transfer is defined as the ratio of Sh at a finite fin mass conductance to that at $\Omega_{\text{Lat}} = \infty$, or

$$\eta_{\text{fin}} = \frac{\text{Sh}_{\Omega_{\text{Lat}}}}{\text{Sh}_{\Omega_{\text{Lat}}=\infty}} \qquad (55)$$

As the mass transfer equations are in the same forms as the heat transfer equations, fin efficiency for mass transfer will equal to that for heat transfer, if the fin mass conductance parameter is equal to the fin heat conductance parameter.

Table 2 lists the obtained Nu and/or Sh and fin efficiencies for various aspect ratios and fin conductance parameters. They are the basic data that can be used for compact heat exchanger or total heat exchanger design.

The fin heat conductance parameters are determined by duct geometry and heat conductivity of fin materials. Table 3 lists the values of fin heat conductance parameters for some frequently encountered materials, including metal and non-metals, for a sinusoidal duct of height 2 mm, aspect ratio 0.5, and fin thickness 0.1 mm. As seen, for almost all the metals, the fin heat conductance parameters are larger than 100, and the resulting fin heat

**Table 2**
Fully developed Nusselt or Sherwood numbers and fin efficiencies for plate-fin sinusoidal ducts.

| $\tau_1$ | $\Omega$ | Nu or Sh | $\eta_{\text{fin}}$ | $\tau_1$ | $\Omega$ | Nu or Sh | $\eta_{\text{fin}}$ |
|---|---|---|---|---|---|---|---|
| 0.2 | ∞ | 1.551 | 1.0 | 0.5 | ∞ | 2.181 | 1.0 |
| | 25 | 1.523 | 0.982 | | 25 | 2.133 | 0.978 |
| | 10 | 1.201 | 0.774 | | 10 | 2.107 | 0.966 |
| | 5 | 1.033 | 0.666 | | 5 | 1.908 | 0.875 |
| | 2 | 0.863 | 0.556 | | 2 | 1.524 | 0.699 |
| | 1 | 0.791 | 0.510 | | 1 | 1.260 | 0.578 |
| | 0.5 | 0.739 | 0.476 | | 0.5 | 1.055 | 0.484 |
| | 0.1 | 0.694 | 0.447 | | 0.1 | 0.824 | 0.378 |
| | 0 | 0.641 | 0.413 | | 0 | 0.737 | 0.338 |
| 1 | ∞ | 2.521 | 1.0 | 2.0 | ∞ | 2.888 | 1.0 |
| | 25 | 2.492 | 0.988 | | 25 | 2.714 | 0.940 |
| | 10 | 2.369 | 0.940 | | 10 | 2.651 | 0.918 |
| | 5 | 2.167 | 0.860 | | 5 | 1.922 | 0.666 |
| | 2 | 1.721 | 0.683 | | 2 | 1.511 | 0.523 |
| | 1 | 1.379 | 0.547 | | 1 | 1.194 | 0.413 |
| | 0.5 | 1.081 | 0.429 | | 0.5 | 0.926 | 0.321 |
| | 0.1 | 0.751 | 0.298 | | 0.1 | 0.631 | 0.218 |
| | 0 | 0.576 | 0.228 | | 0 | 0.358 | 0.124 |
| 5.0 | ∞ | 2.586 | 1.0 | 5.0 | 1 | 1.015 | 0.392 |
| | 25 | 2.390 | 0.924 | | 0.5 | 0.833 | 0.322 |
| | 10 | 2.170 | 0.839 | | 0.1 | 0.661 | 0.256 |
| | 5 | 1.654 | 0.640 | | 0 | 0.173 | 0.067 |
| | 2 | 1.274 | 0.493 | | | | |

*Notes*: $\tau_1$, Duct aspect ratio.

**Table 3**
Values of fin heat conductance parameter for some fin materials with duct height, 2 mm; aspect ratio 0.5, fin thickness, 0.1 mm; fluid, air.

| Fin materials | $\lambda_{fin}$ (W m$^{-1}$ K$^{-1}$) | $\Omega_{sen}$ |
|---|---|---|
| Pure copper | 401 | 751.00 |
| Bronze | 52 | 97.40 |
| Iron | 80.2 | 150.20 |
| Steel | 60.5 | 113.30 |
| Aluminum | 237 | 443.90 |
| Carbon | 1.6 | 3.00 |
| Plywood | 0.12 | 0.22 |
| Wood | 0.16 | 0.30 |
| Clay | 1.3 | 2.43 |
| Glass | 1.4 | 2.66 |
| Paper | 0.18 | 0.34 |
| Teflon | 0.35 | 0.66 |
| Polymer membrane | 0.13 | 0.24 |

*Notes*: $\lambda_{fin}$, Fin heat conductivity; $\Omega_{sen}$, fin heat conductance parameter.



**Fig. 18.** Cross-corrugated triangular ducts.

efficiencies can be as high as 0.90–0.98. For such traditional metal compact heat exchangers, the influences of finite fin heat conductance on heat transfer are negligible. Direct utilization of heat transfer properties for a common duct is acceptable. For the investigated compact total heat exchangers which use non-metals to simultaneously transfer heat and moisture, the fin heat conductance parameters are usually less than 1.0, and the resulting fin efficiencies for heat transfer can be as low as 0.40. Though it's true that the fins still participate in the heat transfer enhancement, at least partially, at this stage, the effects of finite fin heat conductance on heat transfer will be substantial.

The values of fin mass conductance parameters are in the order of $10^{-3}$. With such low mass conductance parameters, the fin efficiencies for mass transfer will be below 0.1–0.2. Under such circumstances, nearly all the mass transfer between the two air streams will be accomplished by the plate, rather than by the fins. The fins seem to behave only like supporting materials, if excluding their role in partial participation in heat transfer. In engineering, sometimes supporting materials or spacers are necessary to separate the two streams because the plates are thin and soft.
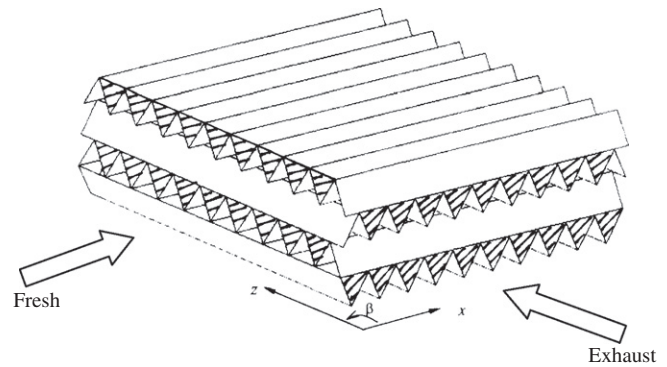
### 4.3. Cross-corrugated ducts [61–63]

#### 4.3.1. Configurations

Parallel plates and plate-fin ducts have been the main structure for total heat exchangers. Parallel-plates are simple, however their heat mass transfer capability is limited. Plate-fin is strong, stable and compact. However as discussed in previous section, due to the finite fin conductance both for sensible heat and latent heat, the fin efficiency is quite limited as well.

To enhance the heat and mass transfer, a structure named the cross-corrugated triangular duct has been proposed [61–63]. It belongs to a type of primary surface heat exchangers, which have been used for air-to-air sensible heat exchangers. The concept is shown in Fig. 18. Flat membrane sheets are corrugated to form a series of parallel equilateral triangular ducts. Sheets of the corrugated plates are then stacked together to form a 90° orientation angle between the neighboring plates, which guarantees the same flow pattern for both fluids. The shaded area is blocked. The structure gives better heat mass transfer. This efficiency improvement is attributed to the pattern of flow that undergoes abrupt turnaround, contraction, and expansion.

Cross corrugated ducts with sinusoidal cross sections, which are mainly used for rotary regenerators, have been investigated extensively by various investigators. Cross-corrugated ducts which have simultaneous heat and mass transfer are studied here. Triangular cross sections are naturally formed by the corrugations of

ultra-thin materials like paper, plastic films, tinsel, and hydrophilic membranes, which are increasingly used in air conditioning industries, due to their superiorities in weight-lightness, cheapness, and abilities in selective transfer.

#### 4.3.2. Fluid flow and heat mass transfer

The flow in the cross corrugated duct is rather complex because of periodic convergent-divergent nature. Various studies have found that transitions from laminar to turbulence occur at Reynolds numbers as low as 150–500, much lower than conventional flat-plates ducts. Due to the small characteristic length and relative low air velocity (<5 m/s), typical Reynolds numbers for a cross-corrugated total heat exchanger are in the range of 100–6000. It is therefore not wise to use a simple laminar modeling technique. In contrary, since the flow in the duct is transitional, numerical modeling should take into account of the turbulence behaviors in the geometry. This is the approach undertaken.

The fluid flow is described by conservation of mass (the continuity equation), momentum (Navier–Stokes equations) and energy (the temperature equation for the fluid) [62]. It would be impossible to solve these equations analytically because of non-linearity and the stochastic nature of turbulence. The extra terms that appear due to averaging the velocity and temperature are the Reynolds stress and the turbulent heat flux. Modeling these is known as the closure problem of turbulence. Various turbulence models have been proposed and totally 4 models are considered. It is found that the Low Reynolds $k$–$\omega$ (LKW) model is the best one for this structure.

Fig. 19 shows the velocity vectors in the mid $y$–$z$ plane. This plane is perpendicular to the main flow direction, and is located at the center of the unit cell. It can be seen that the flow is rather complex, but with regular and interesting patterns. There are strong double swirls in the corner regions of the lower wall, which rotate in a clockwise and a counter-clockwise manner, respectively. The secondary flows in the upper corrugation are relatively weak. In summary, in the upper corrugations, parallel flows are predominant, while in the lower corrugation, secondary swirl flows are dominant. These secondary flows generated swirls will intensify momentum and heat transfer. It is found that a 20–40% of heat transfer enhancement is obtained.

The cyclic mean friction factors under various Reynolds numbers for the developed flow are calculated. The friction factor decreases drastically with Re when the Re is below 2000, but decreases gradually afterwards. A correlation has been formulated to reflect the $f$–Re relations as

$$f = 6.5336 \text{Re}^{-0.421} \tag{56}$$

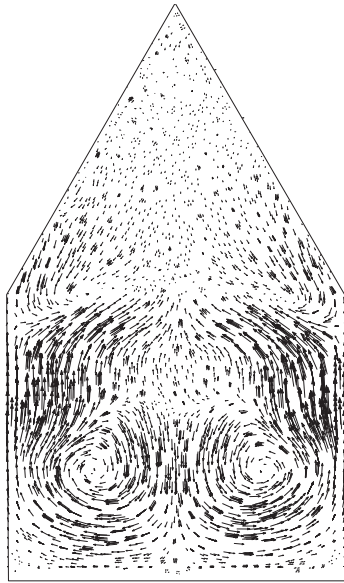where the friction factor, $f$, is defined by the following equation

**Fig. 19.** Velocity vectors in *y–z* mid plane.

$$\Delta P = f \cdot L \cdot \frac{\rho_a}{2} \frac{u_a^2}{d_h} \tag{57}$$

Two correlations are proposed for estimating Nusselt numbers under uniform temperature and uniform heat flux boundary conditions. They are:

$$Nu = 0.1922 Re^{0.599} Pr^{0.333} \tag{58}$$

for uniform temperature, and

$$Nu = 0.2743 Re^{0.569} Pr^{0.333} \tag{59}$$

for uniform heat flux conditions, respectively.

For mass transfer

$$Sh = 0.266 Re^{0.539} Sc^{0.333} \tag{60}$$

Four total heat exchangers are designed and constructed. They are: (1) parallel plates duct structure with homogeneous polymer membrane; (2) parallel plates duct structure with composite supported liquid membrane (CSLM); (3) cross-corrugated triangular duct structure with homogeneous polymer membrane; and (4) cross-corrugated triangular duct structure with CSLM. The struc-

tural parameters and operating conditions are the same: 115 channels for each flow, channel pitch 2 mm, channel length 185 mm, each membrane 185 × 185mm$^2$.

Experiments are done. Table 4 lists the heat and mass transfer properties of the four total heat exchangers. As seen, the cross-corrugated structure intensifies air side convective heat and mass transfer substantially. Compared to a parallel-plates duct, the convective heat and mass transfer coefficients in a cross-corrugated duct increased by 22%. Besides, transfer area increased by 2-folds. These two factors make the new structure more compact and have a higher heat mass transfer capabilities. As a penalty, the pressure drop increased from 12 Pa to 71 Pa.

Compared to a common homogeneous membrane, the composite supported liquid membrane has a 46% less membrane side mass transfer resistance. Consequently, the CSLM could increase latent effectiveness by 8%, even with the same traditional parallel-plates duct structure. The effect of CSLM on decreasing heat transfer resistance is not obvious, since the dominant resistance in the unit is in air side. However, when the CSLM is combined with the cross-corrugated triangular duct, it will have the highest sensible effectiveness of 0.82, and the highest latent effectiveness of 0.64, which is highly desired in market.

### 4.4. Hollow fibers module [64]

#### 4.4.1. Configuration

Hollow fiber membranes are a promising alternative. In this concept, as shown in Fig. 20, a bundle of hollow fiber membranes is packed in a shell to form a module. The structure is like a shell-and-tube heat exchanger. The fresh air and the exhaust air flow in the tube side and shell side respectively. They exchange heat and moisture through the membrane wall. The membrane-made fibers are in a diameter of 1–3 mm, so the packing density is rather high. The contact area between the two air streams can be as high as 1000 m$^2$/m$^3$. As a result, the heat and moisture exchange effectiveness can be high enough to attract commercial interests.

#### 4.4.2. Heat mass transfer in the module

Fresh air flows in tube side. For laminar flow in round tubes, the product of friction factor and Reynolds number satisfies

$$(f \cdot Re) = 64 \tag{61}$$

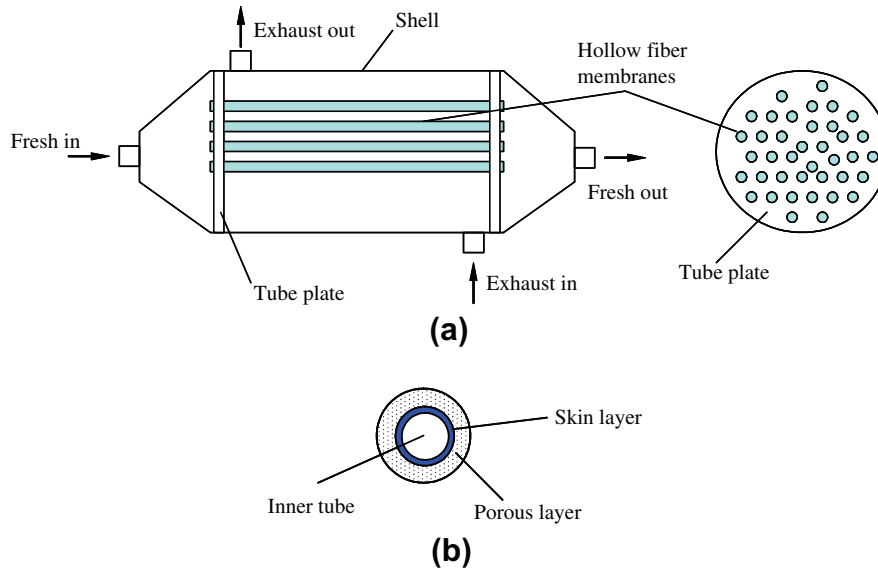Mass transfer inside hollow fiber membranes is governed by

$$Sh = 1.62 \left( \frac{d_i^2 u_i^2}{L D_{va}} \right)^{1/3} \tag{62}$$

**Table 4**
Performance comparison of four total heat exchanger configurations.

| Structure | Case 1 Parallel-plates | Case 2 Parallel-plates | Case 3 Cross-corrugated | Case 4 Cross-corrugated |
|---|---|---|---|---|
| Membrane | Homogeneous | CSLM | Homogeneous | CSLM |
| $d_h$ (mm) | 3.96 | 3.96 | 2.0 | 2.0 |
| Re | 249 | 249 | 126 | 126 |
| Nu | 7.54 | 7.54 | 4.67 | 4.67 |
| Sh | 7.10 | 7.10 | 4.39 | 4.39 |
| $h_f$, $h_e$ (kW m$^{-2}$ K$^{-1}$) | 0.05 | 0.05 | 0.061 | 0.061 |
| $k_f$, $k_e$ (m/s) | 0.051 | 0.051 | 0.062 | 0.062 |
| $f$ | 0.3855 | 0.3855 | 1.1856 | 1.1856 |
| $A_{tot}$ (m$^2$) | 8.0 | 8.0 | 16.0 | 16.0 |
| $NTU_{sen}$ | 4.15 | 4.15 | 10.0 | 10.0 |
| $NTU_{Lat}$ | 1.08 | 1.65 | 1.42 | 2.29 |
| $\varepsilon_{sen}$ | 0.72 | 0.72 | 0.82 | 0.82 |
| $\varepsilon_{Lat}$ | 0.47 | 0.57 | 0.55 | 0.64 |
| Pressure drop (Pa) | 12 | 12 | 71 | 71 |

*Notes*: CSLM, Composite supported liquid membrane.

**Fig. 20.** Schematic of the hollow fiber membrane module for heat and moisture recovery. (a) The shell and tube structure and (b) structure of a single membrane fiber.

Exhaust air flows in shell side. Established correlation for mass transfer in shell side of a hollow fiber membranes module is

$$\text{Sh} = (0.53 - 0.58\varphi_1)\text{Re}^{0.53}\text{Sc}^{0.33} \tag{63}$$

where $\varphi_1$ is the packing fraction of the module, which is the ratio of total cross sectional area of the fibers to the module.

$$\varphi_1 = \frac{N_{\text{fr}}d_0^2}{D_0^2} \tag{64}$$

where $D_0$ is the diameter of the module shell (m); $d_0$ is the outer diameter of a single fiber (m); $N_{\text{fr}}$ is the number of fibers in the module.

The air flow area in shell side

$$A_{\text{flow}} = (1 - \varphi_1) \cdot \frac{\pi D_0^2}{4} \tag{65}$$

The hydrodynamic diameter in shell side is defined to four times of flow area divided by total perimeter of membrane fibers

$$d_{\text{h}} = \frac{4A_{\text{flow}}}{N_{\text{fr}}\pi d_0} = \frac{(1 - \varphi_1)D_0^2}{N_{\text{fr}}d_0} \tag{66}$$

Resistance through the shell side is measured. It is related to packing density and flow configurations. A correlation can be summarized to estimate the product of friction factor and Reynolds number as

$$(f \cdot \text{Re}) = 41.3 \tag{67}$$

Resistances from fresh air to exhaust air can be considered as a sum of resistances in series. The overall mass and heat transfer coefficients from fresh to exhaust air on the basis of outer surface of the fibers are calculated by

$$\frac{1}{K} = \frac{1}{k_{\text{i}}}\left(\frac{d_0}{d_{\text{i}}}\right) + \frac{\delta}{D_{\text{vm}}}\left(\frac{d_0}{\bar{d}}\right) + \frac{1}{k_{\text{o}}} \tag{68}$$

$$\frac{1}{U} = \frac{1}{h_{\text{i}}}\left(\frac{d_0}{d_{\text{i}}}\right) + \frac{\delta}{\lambda_{\text{m}}}\left(\frac{d_0}{\bar{d}}\right) + \frac{1}{h_{\text{o}}} \tag{69}$$

where $\bar{d}$ is the arithmetic mean diameter of a fiber, i.e., $(0.5 * (d_{\text{o}} + d_{\text{i}}))$.

When the overall heat and mass transfer coefficients are calculated, the $\varepsilon$–$NTU$ method developed previously can be used to estimate the sensible and latent effectiveness of the module. The number of fibers packed $N_{\text{fr}}$, has a great influence on performance. Fig. 21 shows the effects of the number of fibers on $NTU_{\text{sen}}$ and $NTU_{\text{Lat}}$, and on the consequent sensible and latent effectiveness. The inner diameter of the fiber is fixed to 1.2 mm. The number of the fiber, $N_{\text{fr}}$, influences the exchange area directly. As seen, when $N_{\text{fr}}$ is increased from 50 to 250, the $NTU_{\text{sen}}$ increases from 1.06 to 5.93, while the $NTU_{\text{Lat}}$ increases form 0.64 to 3.4. Correspondingly, the sensible effectiveness increases from 0.52 to 0.86, while the latent effectiveness increases from 0.39 to 0.77.

On the other hand, the value of $NTU_{\text{Lat}}$ is generally less than that of $NTU_{\text{sen}}$. When the $N_{\text{fr}}$ is increased from 50 to 250, the overall Lewis number ($Le_{\text{tot}} = Nu_{\text{sen}}/Nu_{\text{Lat}}$) varies from 0.60 to 0.57. The variations are relatively small.

For this structure, special care should be taken to pressure drop considerations, because the resistance is relatively large.

## 5. Novel insights: performance deteriorations from flow maldistribution [65–67]

### 5.1. Real distribution

The exchanger core (or element) cannot work alone. Besides exchanger core, ducts, inlet/outlet vents and fans are necessary to assemble a practical product. Fig. 22 shows the schematic of a practical total heat exchanger. As seen, the whole exchanger is
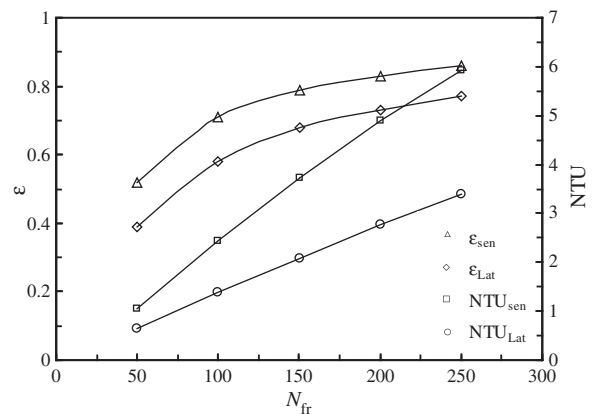


**Fig. 21.** Effects of the number of fibers on performance, $d_{\text{i}}$ = 1.2 mm.

composed of inlet vents, outlet vents, exchanger shells, separating plates, and most importantly, the core. When installed, the exchanger core is rotated 45° and inserted into the exchanger shell, forming two parallel air ducts with the separating plates in the rectangular shell box. Fresh air is sucked into the exchanger by a fan (not shown in the figure) through the fresh air inlet. Exhaust air is sucked into the exchanger by another fan through the exhaust air inlet. The two air streams are driven through the exchanger core in a cross-flow arrangement. Due to the complex structure, flow maldistribution exists on the core face.

The maldistribution can be analyzed with a definition of local flow nonuniformity parameter as

$$\beta = \frac{\dot{m}}{\dot{m}_m} \tag{70}$$

where $\dot{m}$ is the actual local mass flow rate (kg m$^{-2}$ s$^{-1}$), and $\dot{m}_m$ is the average mass flow rate across the core face. When the air is considered as incompressible fluid, the nonuniformity can be simply calculated as the local to mean velocity ratio.

The exchanger thermal and latent performance deterioration factors are defined by

$$\theta_{sen} = \frac{\varepsilon_{sen,uniform} - \varepsilon_{sen}}{\varepsilon_{sen,uniform}} \tag{71}$$

$$\theta_{Lat} = \frac{\varepsilon_{Lat,uniform} - \varepsilon_{Lat}}{\varepsilon_{Lat,uniformm}} \tag{72}$$

where $\varepsilon_{sen,uniform}$ and $\varepsilon_{Lat,uniform}$ are exchanger sensible and latent effectiveness at uniform flow distribution, respectively.

A CFD code is used to model the flow distribution in the exchanger. The modeling geometry is shown in Fig. 23. There are three volumes: inlet duct, outlet duct, and the core. The core is treated as a porous media. It is one dimensional for parallel plates and two dimensional for parallel-plates structure. The flow in core channels is unmixed flow. After the calculation flow fields, the heat and moisture transfer is modeled with a self built meso-scale model.

## 5.2. Parallel-plates core

Three cores with different channel pitches are considered: A, 3.5 mm; B, 2.5 mm; and C 1.8 mm. The profiles of velocity nonuniformity (local to mean velocity ratio) on core outlet face for Core B is shown in Fig. 24. The larger the channel pitch is, the more serious the flow maldistribution is. The maximum flow nonuniformity for 3.5 mm pitch Core A is 3.7, while only 1.9 for 1.8 mm pitch Core C. For all cores, the highest velocity exists at the center of the core face where the incoming fluids impinge on the core face directly. The least velocity exists on the corners of the core surface, because here the pressure is the least. The flow maldistribution is co-determined by the inlet duct, the core and the outlet duct. The core itself plays a determinant role in the flow maldistribution. These components should be coupled together to predict the flow maldistribution. When the core channel pitch is below 2 mm, a semi-uniform flow distribution can be assumed. On the other hand, flow maldistributions on cores with channel pitches larger than 2 mm are very serious. They should be taken into account.

For engineering applications, the overall heat and moisture exchange effectiveness of the whole exchanger is significant. Table 4 lists the exchanger thermal and latent performance deterioration factors under various air flow rates for the three cores. As can be seen, both the thermal and the latent performance deterioration factors for the Core C are within 9% and the performance deterioration can be neglected. However, for the two cores with larger channel pitches, the performance deteriorations are substantial. The deterioration factors for Core A can be as high as 28%. For all the three cores, both the sensible and the latent effectiveness are equally influenced. In contrast, for plate-fin cores, the sensible and latent effectiveness deteriorations are around 15% even with a large pitch of 4 mm. Therefore compared to plate-fin cores, parallel-plates cores should be paid to more attention on the problem of flow maldistribution.

For parallel-plates compact heat exchanger cores, the channel pitch determines how serious the flow maldistribution is. For the current structure, when the channel pitch is larger than 2 mm, the flow maldistribution becomes serious and the nonuniformity
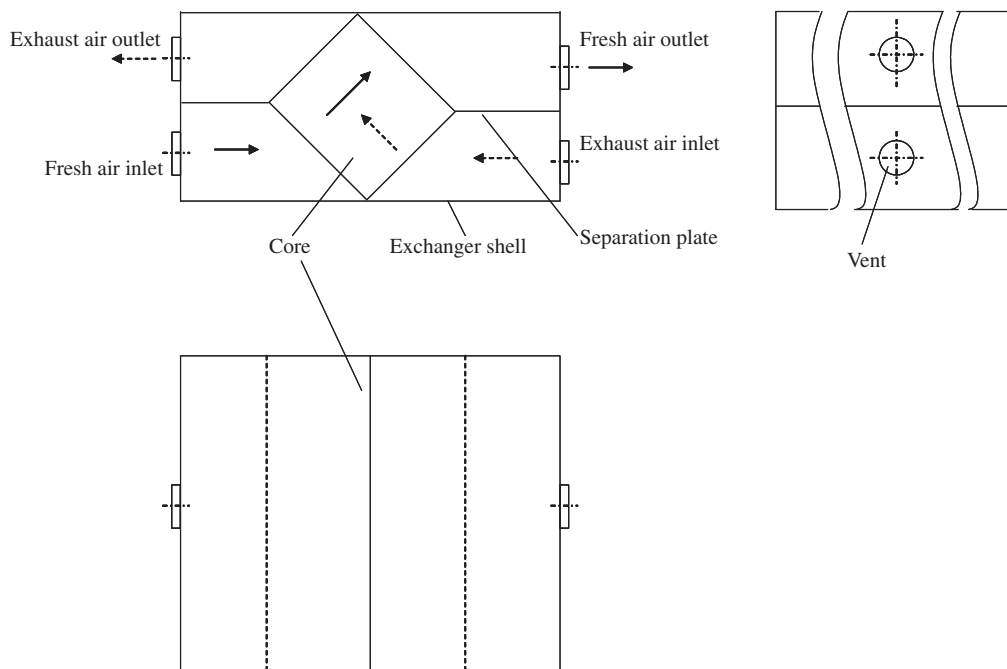


**Fig. 22.** Schematic of a real cross-flow air to air total heat exchanger.
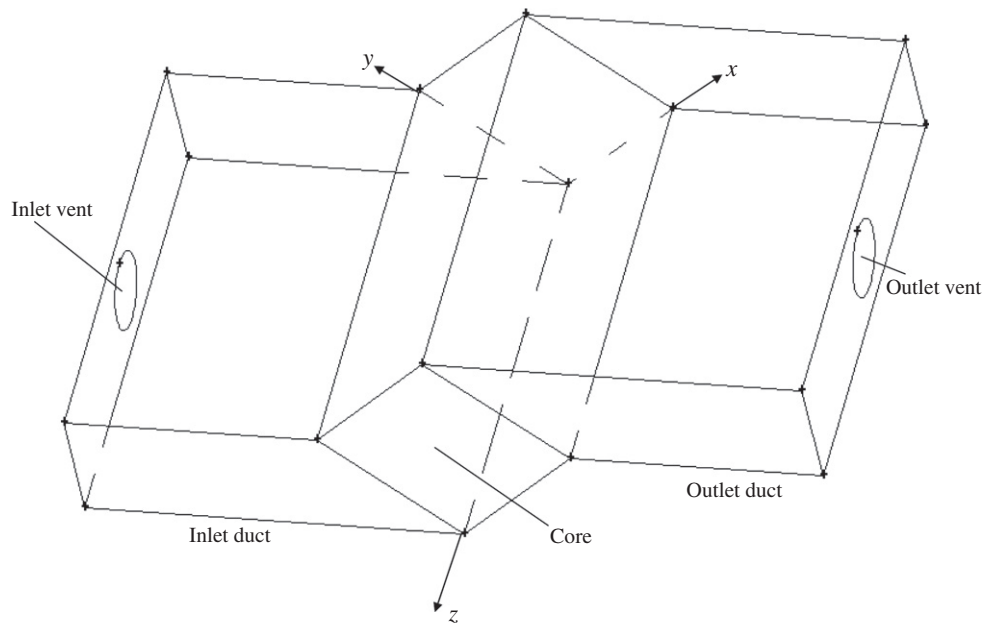
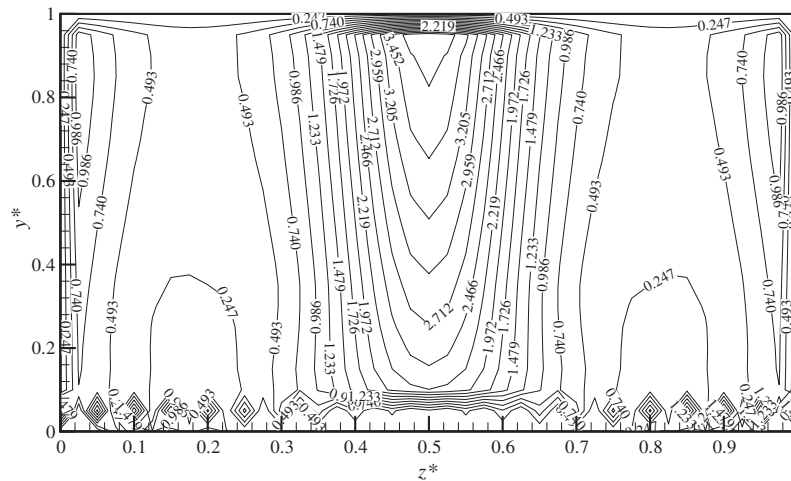Fig. 23. The calculating geometry for flow maldistribution.



Fig. 24. Velocity nonuniformity on exchanger core face, channel pitch 2.5 mm, parallel-plates core.

problem should be considered. The sensible and latent effectiveness can be deteriorated by 28%. Table 5.

### 5.3. Plate-fin core

The effects of the core channel pitch on flow maldistribution are modeled, with plate-fin structures. As before, three channel pitches are considered: A (2.5 mm), B (1.8 mm), and C (4 mm). The profiles of velocity nonuniformity on core outlet face for the Core B are plotted in Fig. 25. The flow distributions on the core inlet face are the same as those on outlet face, since only one dimensional flow on channel length is permitted.

The larger the channel pitch is, the more serious the flow maldistribution is. When the core channel pitch is below 2 mm, a uniform flow distribution can be assumed. This is easy to understand. A core with such small channels is just like a flow straightener. Flow after such equipments becomes uniform. On the other hand, flow maldistributions on cores with channel pitches larger than 2 mm are very serious. They should be taken into account.

Fig. 26 depicts the exchanger thermal and latent performance deterioration factors under various air flow rates for the three plate-fin cores. As can be seen, both the thermal and the latent performance deterioration factors for the Core C are very small and the performance deterioration can be neglected. However, for the two cores with larger channel pitches, the performance deteriorations are substantial. The deterioration factors for Core B are the highest among the three. The sensible effectiveness is decreased by 15–20%, and the latent effectiveness is decreased by 20–25%. The higher deterioration factors for latent effectiveness are due to the higher moisture resistance through membranes. Compared to sensible-only heat exchangers, enthalpy exchangers should be paid to more attention for flow maldistribution. Latent effectiveness of a total heat exchanger is usually small. A uniform flow distribution becomes more important because all the exchanger area should be equally and sufficiently employed to take part in moisture exchange.

The flow maldistribution is determined by channel to whole exchanger pressure drop ratio. When the channel pitch is less than

**Table 5**
Sensible and latent effectiveness and deterioration factors for three cores.

| $V$ (m³/h) | Sensible effectiveness | | | Latent effectiveness | | |
|---|---|---|---|---|---|---|
| | $\varepsilon_{sen,uniform}$ | $\varepsilon_{sen}$ | $\theta_{sen}$ | $\varepsilon_{Lat,uniform}$ | $\varepsilon_{Lat}$ | $\theta_{Lat}$ |
| *Core A, 2a = 3.5 mm* | | | | | | |
| 100 | 0.59 | 0.46 | 0.230 | 0.58 | 0.45 | 0.234 |
| 125 | 0.55 | 0.42 | 0.246 | 0.54 | 0.40 | 0.251 |
| 150 | 0.51 | 0.39 | 0.245 | 0.50 | 0.38 | 0.250 |
| 175 | 0.48 | 0.36 | 0.260 | 0.47 | 0.35 | 0.265 |
| 200 | 0.46 | 0.33 | 0.281 | 0.44 | 0.32 | 0.280 |
| *Core B, 2a = 2.5 mm* | | | | | | |
| 100 | 0.69 | 0.60 | 0.130 | 0.67 | 0.58 | 0.134 |
| 125 | 0.66 | 0.56 | 0.152 | 0.64 | 0.54 | 0.156 |
| 150 | 0.63 | 0.53 | 0.159 | 0.61 | 0.51 | 0.164 |
| 175 | 0.61 | 0.50 | 0.180 | 0.58 | 0.48 | 0.172 |
| 200 | 0.59 | 0.48 | 0.186 | 0.56 | 0.46 | 0.179 |
| *Core C, 2a = 1.8 mm* | | | | | | |
| 100 | 0.76 | 0.72 | 0.053 | 0.73 | 0.69 | 0.055 |
| 125 | 0.74 | 0.69 | 0.068 | 0.71 | 0.66 | 0.070 |
| 150 | 0.72 | 0.67 | 0.070 | 0.69 | 0.64 | 0.073 |
| 175 | 0.70 | 0.65 | 0.071 | 0.67 | 0.62 | 0.075 |
| 200 | 0.68 | 0.63 | 0.074 | 0.65 | 0.59 | 0.092 |

*Notes*: $V$, Air flow rate; $\varepsilon$, effectiveness; $\theta$, deterioration factor.



**Fig. 26.** Performance deterioration factors for the three cores under various air flow rates, plate-fin core.

2 mm, the flow maldistribution is very small and can be neglected. When the channel pitch is larger than 2 mm, the flow maldistribution becomes serious and the nonuniformity problem should be considered. This 2 mm limit would depend on the geometric details such as width and depth of the core. The cores of small pitches have larger pressure resistance, which could offset some degree of flow maldistribution that is generated by irregular duct geometries like turnaround, expansion, and contraction.
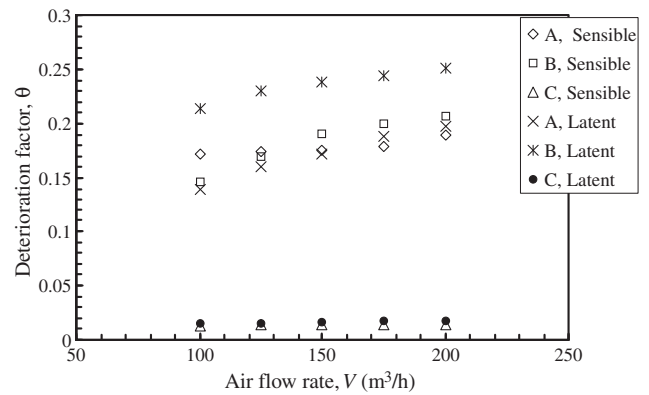
Generally, however, the flow maldistribution for plate-fin structure is not as serious as parallel-plates structure. Therefore, the flow maldistribution for parallel-plates core is more serious than that for plate-fin core. Special attention should be given to parallel-plates core.

# 6. Novel systems

## 6.1. Chilled-ceiling with total heat recovery

### 6.1.1. Desiccant cooling (DC) with chilled-ceiling [21–24]

This is a de-coupled cooling strategy. The schematic of the system components is shown in Fig. 27. Chilled-ceiling panels are equipped to extract sensible load, and dehumidified fresh air is supplied by a desiccant cooling system. The principles of the desiccant cooling cycle are well-known. Ambient outdoor air at state 1 enters the supply air duct. This air passes through a desiccant wheel and hot, dry air exits at state 2. This increase in temperature is due to the heat of sorption and some sensible heat transfer. The hot, dry supply air transfers much of this heat to the return air stream in process 2–3 involving a sensible heat wheel. Unlike a commonly used desiccant cooling, where air at state 3 is evaporatively cooled to state 4, in this system, the warm, dry air at state 3 is cooled by a cooling coil, to keep the dryness of supply air at state 4. The cool, dry air at state 4 is then distributed to the room. After accepting the building latent load and a small amount of sensible load, the air then returns to the desiccant system through return air ducting. This is the state of the air which corresponds to state 5. This somewhat cool, fairly dry air is evaporatively cooled to as low a temperature as possible at state 6. This cold, damp air is then preheated by the rotary sensible wheel to state 7 while cooling the supply air stream. State 7 is the state of the moist air as it enters the heating coil. Hot, humid air exits at state 8 and regenerates the desiccant wheel. Warm, very humid air at state 9 is then exhausted to the surroundings. Chilled water flows through the cooling coil and chilled ceiling panels in series, implying that only one refrigerator with an evaporating temperature as high as 15 °C is needed. In this scheme, partial total heat recovery is realized by the evaporative cooling of exhaust air.
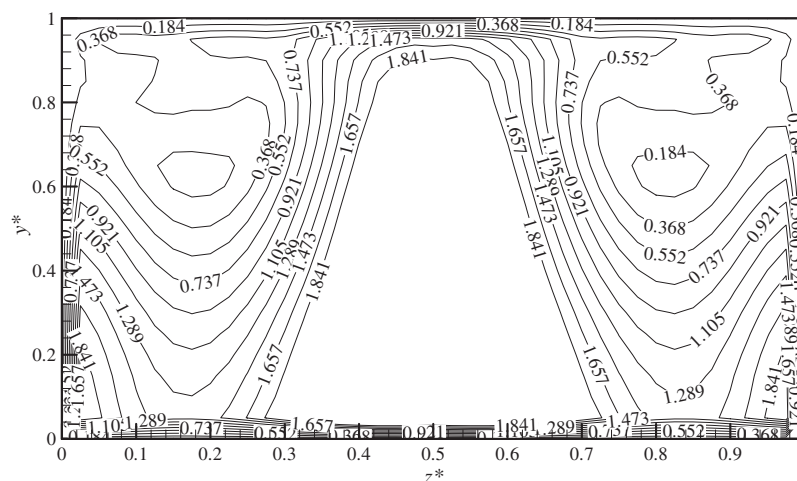


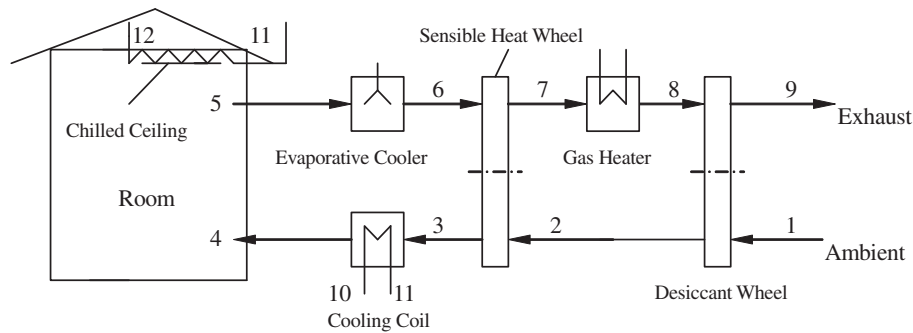**Fig. 25.** Velocity nonuniformity on exchanger core face, channel pitch = 2.5 mm, plate-fin core.

**Fig. 27.** A desiccant cooling combined with chilled-ceiling.

Ventilation distribution is provided by displacement ventilation. Displacement ventilation brings air into the space near floor level at a low velocity and air is exhausted at the ceiling. This strategy delivers fresh air to where the occupants require it and odors and airborne contaminants are carried to the ceiling and exhausted instead of being recirculated as is common with traditional HVAC systems.

Research found that Chilled-ceiling combined with desiccant cooling could save up to 44% of primary energy, in comparison with a constant volume all-air system. In addition, with chilled-ceiling, temperature and humidity control have been decoupled by using desiccant wheel for moisture removal and ceiling for temperature control [24]. The problem with this system is that it is complicated and it is only suitable for large scale systems.

### 6.1.2. Pre-cooling desiccant cycle with chilled-ceiling [68]

It is discovered that in hot and humid regions, very high regenerating temperatures are required, otherwise the performance of the desiccant system would deteriorate seriously in extreme weather conditions. To address this problem, a modification of a desiccant cycle, a pre-cooling desiccant cooling cycle (PCDC), has been proposed and combined with chilled ceiling panels for an office building. A PCDC cycle could use lower regenerating temperatures in comparison with a DC cycle.

Fig. 28 illustrates a schematic of this cycle. The components are similar to a DC cycle, but an additional total heat exchanger, which is a membrane-based total heat exchanger, is added to the system. Ambient air at state 1 first passes through a total heat exchanger where it exchanges sensible heat and moisture with the exhaust air. Air at state 2 then passes through the rotating dehumidifier matrix and hot, dry air exits at state 3. The hot, dry supply air transfers much of its heat to the return air stream in process 3–4 involving a sensible heat wheel. The warm, dry supply air at state 4 is now cooled by a cooling coil to state 5 and is supplied to the conditioned space.

After accepting the building latent load and some sensible load, the air then returns to the air ducting. This room air, which is still relatively cool and dry, is first ushered into the total heat exchanger to pre-cool and pre-dry the outside fresh air, through process 6–7. Air exited from the total heat exchanger at state 7 is evaporatively cooled to state 8 and is used to cool the supply air in the sensible heat exchanger involving process 8–9. The air at this stage is further heated by a gas heater to state 10 and is used to regenerate the desiccant wheel. After passing through the regenerating desiccants matrix passages, air becomes hot and humid and is exhausted to the outside.

The temperature of the return air at state 9 required to regenerate the desiccant is a property of the type of desiccant used and the amount of dehumidification required in process 2–3. This system takes full use of the total heat recovery.

The system is investigated [68]. It is found that pre-cooling improves wheel's dehumidification efficiency, therefore, lower regenerating temperatures can be employed with a PCDC cycle. The more humid it is, the more superior a PCDC in comparison with a DC cycle. With a PCDC cycle, nearly 99% of annual operating hours are with less than 80 °C regenerating temperatures. In contrast, a common DC cycle needs 30% annual hours' heat of higher than 80 °C.

The proposed PCDC system is a step forward for more efficient, energy saving system, which could be used in hot and humid regions. The problem is that the system is still complicated and small machines for household use are not easy.

### 6.2. Fresh air dehumidification with total heat recovery [69–72]

Previous studies reveal that desiccant cooling combined with total heat recovery are promising for humidity control and energy saving in hot and humid regions. However they are bulky and additional outside heat sources are required, which is not easy for densely populated urban areas like Guangzhou.

To address the problem, recently, a fresh air refrigeration dehumidification system with membrane total heat exchanger is investigated and built in our laboratory. The system comprises of all the necessary parts for real application. A detailed mathematic model based on cell-by-cell approach has been developed to optimize the system [71,72]. Experiments are conducted to validate the model. Then the effects of operating conditions on the dehumidification capacity and the coefficient of performance are investigated. The results help to optimize the demonstrative unit.

The theory is that in this system, a membrane based total heat exchanger is used before the fresh air is pumped to a heat pump for air dehumidification. The total heat exchanger has a membrane core where the incoming fresh air exchanges moisture and temperature simultaneously with the exhaust air. In this manner, the total heat or enthalpy from the exhaust is recovered. The schematic for this system is shown in Fig. 29. This system is relatively simple, since the membrane system has no moving parts, and is compact. The mechanical refrigeration system is suitable to use in densely populated urban regions like Guangzhou city.

Energy savings effects on a 1-year basis are modeled with the weather conditions in Guangzhou [69,70]. In hot and humid regions like Guangzhou, air dehumidification is required most of the year. The outside temperatures usually exceed 35 °C and humidity exceed 80%RH. The COP of a traditional common refrigerator is usually below 2.8. The new system is modeled. The variations of the yearly COP of the system are shown in Fig. 30. As seen, the COP is greatly improved, in comparison with a traditional system. In most days, it is from 4.0 to 6.8. In addition, energy analysis found that in January and February [70], when it is the dry season, energy requirements are the least energy. In August, it is the
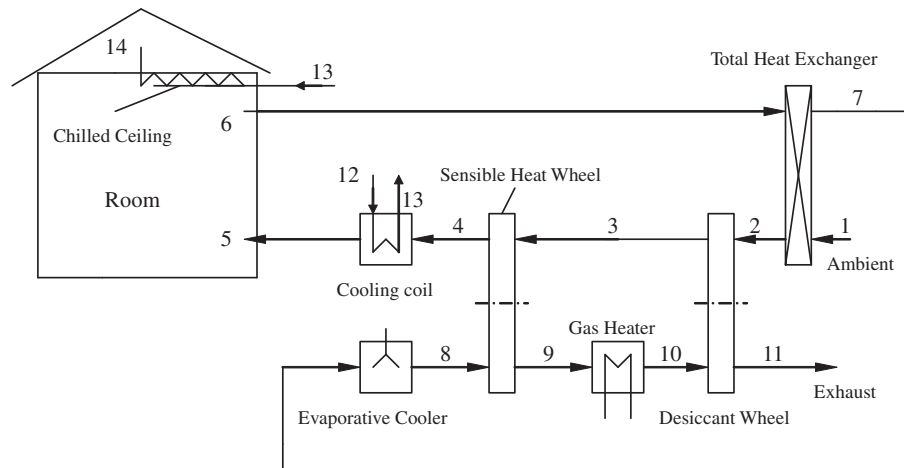
**Fig. 28.** A pre-cooling desiccant cooling combined with chilled-ceiling.
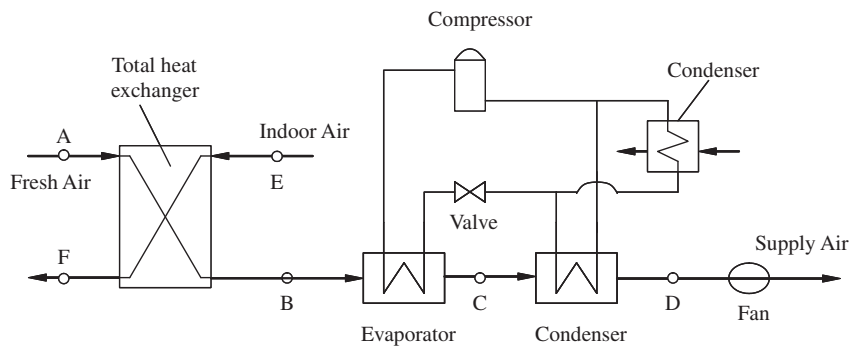


**Fig. 29.** Schematic of mechanical fresh air dehumidification with membrane-based total heat exchanger.

most humid season, required energy is the largest. Five months from May to September account for 60.5% of the yearly energy load. Other 7 months account for the rest 39.5%. South China has a long hot and humid summer. The energy for air dehumidification is substantially large. To save energy while ensuring a healthy built environment with enough fresh air ventilation, an independent air dehumidification system with energy recovery is necessary.

To extend the system in real engineering applications, a demonstrative machine has been built in our laboratory [71]. The picture of the whole machine is shown in Fig. 31. The picture of the membrane total heat exchanger element (core), which can be

inserted in the machine, is shown in Fig. 32. The demonstrative unit has been used in real buildings and is experimented. The results are summarized as following:

(1) The total heat exchanger has a sensible effectiveness of 0.8 and a latent effectiveness of 0.7. The Number of transfer units is 4.2, with 8 m$^2$ composite membranes.
(2) The fresh air dehumidification system has a high air dehumidification rates with a high COP. The air dehumidification rates and COP are 3.57 kg h$^{-1}$ and 5.8, respectively. The test
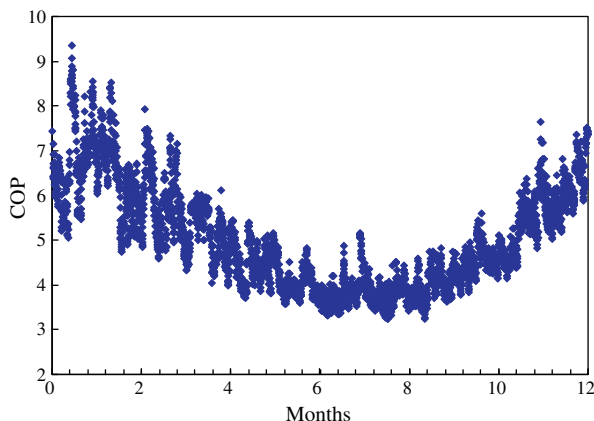


**Fig. 30.** Distribution of COP of the dehumidification system in a year, by hourly simulations.



**Fig. 31.** A demonstrative machine of fresh air dehumidification system with membrane total heat recovery.

conditions are: fresh air temperature 35 °C, fresh air humidity 70%, room temperature 27 °C, room humidity 53%, and supply air temperature 20 °C. The prototype has a fresh air flow rate of 200 m³/h. Comparing with a conventional mechanical dehumidification system, the air dehumidification rate of the proposed system is 3.5 times higher, and the COP is 2.2 times higher. This implicates that the membrane-based total heat exchanger improves the performances greatly. The new system is a promising and efficient air dehumidification system in hot and humid environment.

(3) The new system is more robust than conventional air dehumidification systems under hot and humid harsh weather conditions. The higher the fresh air temperature and humidity are, the more effective the membrane-based total heat exchanger is. Though the performance of the compression sub-system deteriorates as expected under these harsh conditions, the overall performance of the new system surprisingly only deteriorates a little, because the performances of the membrane sub-system are higher. The adverse effects of hot and humid weather conditions on the compression sub-system are offset by the membrane sub-system. This is obviously the benefit of the new system. Further, the system is simple and is suitable for household small machines. Works are undertaken to cut the prices down.

## 7. Cross-over of pollutants and the extension of membrane systems

The heat and mass transfer in novel total heat exchanger structures are continuously searched, both in cross-corrugated triangular ducts [73] and in quasi-counter flow parallel plates [74]. The membrane systems are also extended to other areas, like air humidification [75] and air dehumidification [76]. The heat and mass transfer in hollow fiber membrane contactors, either in counter flow [77], or in cross flow [78], are systematically studied to realize non-contacting liquid desiccant air dehumidification. The work is still being conducted. Further, Recently, a novel membrane, asymmetric membrane has been fabricated to solve the problem of complexity in membrane making process, and to reduce the costs of membranes [79,80]. The membrane making theory has been extended to the fabrication of novel selective adsorbents for desiccant wheels and sorbent beds for heat and moisture recovery [81].

It should be noted that fresh air ventilation is crucial for indoor environmental control. Total heat exchangers are the key equipments for energy conservation in ventilation. Membranes have been used for total heat exchangers for a dozen of years. Much efforts have been spent on water vapor permeability of various membranes, however relatively little attention has been paid to the selectivity of moisture over VOCs through such membranes. A membrane should be a barrier to other unwanted gases like VOCs. In our laboratory, the most commonly used membranes, either hydrophilic ones (PVP, PVA, PAM, Na(Alg), CS, CA, EC) or hydrophobic ones (PP and PDMS), are tested for their permeability of moisture and five VOCs (acetic acid, formaldehyde, acetaldehyde, toluene and ethane) [82]. The selectivity of moisture/VOCs of these membranes is then evaluated. With a solution–diffusion model, the solubility and diffusivity of moisture and VOCs in these membranes are calculated. They could provide some reference for future material selections. Fig. 33 shows the permeability of water vapor and water vapor/Formaldehyde selectivity for the 10 membranes. As seen, the selectivity of vapor/formaldehyde is 200–300 for the membranes developed in this laboratory. This indicates that VOCs cannot permeate the membranes while moisture can. The total heat exchangers are ideal to control indoor air quality, in addition to energy recovery. There is no cross-over problems.

As for the 10 most commonly used membranes, the permeability of water vapor in the 10 membranes decreases in the following order:

$$PVA - 1 > PVP > PAM > Na(Alg) > CS > PVA - 2 > CA > EC$$
$$> PP > PDMS$$

## 8. Conclusions

Conditioning of ventilation fresh air accounts for 20–40% of the total energy cost in air-conditioning industry. Stringent ventilation regulations make the problem more serious. Total heat recovery from ventilation air has become one of the most important fraction of HVAC energy conservation. The energy savings potential is great. However there are full of challenges. The difficulties come from the small temperature and humidity differences between the fresh air and the exhaust air. Novel membranes as well as novel structures should be searched. In heat and mass transfer modeling, novel concepts should be used.

Under these backgrounds, much work in this direction has been conducted in South University of Technology in these years. There has been great progress made in these areas: new material fabrication, new system design, novel heat and mass transfer modeling and system engineering applications. With the newly designed composite membranes, and novel exchanger structures, a total
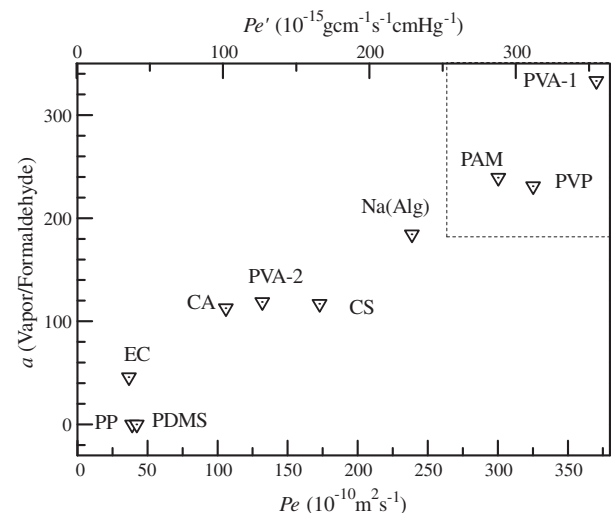


**Fig. 32.** The membrane core (element) used in the novel air dehumidification unit.



**Fig. 33.** Permeability of water vapor and water vapor/formaldehyde selectivity for the 10 membranes.

heat exchanger developed has a sensible effectiveness above 0.8 and latent effectiveness above 0.7. When the developed exchanger is combined to a refrigeration fresh air dehumidification unit, the COP is above 5.8, and dehumidification rates are 3.57 kg/h. The unit has been successfully used in a 200 m² room. About 70–80% of the energy for conditioning fresh air is saved. They provide a solution for sustainable air conditioning systems in hot and humid regions. In future, developing more cost-effective membranes is the direction for commercial applications. The membranes can prevent VOCs leaking. The researches on membranes have been extended to other areas like air humidification and air dehumidification, adsorbents making, and so on.

## Acknowledgements

## References

[1] Zhang YP, Yang R, Zhao RY. A model for analyzing the performance of photocatalytic air cleaner in removing volatile organic compounds. Atmos Environ 2003;37:3395–9.

[2] Mo JH, Zhang YP, Yang R. Novel insight into VOC removal performance of photocatalytic oxidation reactors. Indoor Air 2005;15:291–300.

[3] Xu Y, Zhang YP. An improved mass transfer based model for analyzing VOC emissions from building materials. Atmos Environ 2003;37:2497–505.

[4] Xu Y, Zhang YP. A general model for analyzing VOC emission characteristics from building materials and its application. Atmos Environ 2004;38:113–9.

[5] Liu XH, Zhang Y, Qu KY, Jiang Y. Experimental study on mass transfer performances of cross flow dehumidifier using liquid desiccant. Energy Convers Manage 2006;47:2682–92.

[6] Liu XH, Li Z, Jiang Y, Lin BR. Annual performance of liquid desiccant based independent humidity control HVAC system. Appl Therm Eng 2006;26:1198–207.

[7] Zhang LZ. Total heat recovery: heat and moisture recovery from ventilation air. New York: Nova Science Publishing Co; 2008 [Chapter 1].

[8] Zhang LZ, Jiang Y. Heat and mass transfer in a membrane-based enthalpy recovery ventilator. J Membr Sci 1999;163:29–38.

[9] Zhang LZ, Jiang Y, Zhang YP. Membrane-based humidity pump: performance and limitations. J Membr Sci 2000;171:207–16.

[10] Zhang YP, Jiang Y, Zhang LZ, Jin JF. Analysis of thermal performance and energy saving effect of membrane based heat recovery ventilator. Energy 2000;25:515–27.

[11] Zhang LZ, Niu JL. Energy requirements for conditioning fresh air and the long-term savings with a membrane-based energy recovery ventilator in Hong Kong. Energy 2001;26:119–35.

[12] Wu Z, Melnik RVN, Borup F. Model-based analysis and simulation of regenerative heat wheel. Energy Build 2006;38:502–14.

[13] Nielsen TR, Rose J, Kragh J. Dynamic model of counter flow air to air heat exchanger for comfort, ventilation with condensation and frost formation. Appl Therm Eng 2009;29:462–8.

[14] Adamski M. Longitudinal flow spiral recuperators in building ventilation systems. Energy Build 2008;40:1883–8.

[15] Yau YH. The use of a double heat pipe heat exchanger system for reducing energy consumption of treating ventilation air in an operating theatre – a full year energy consumption model simulation. Energy Build 2008;40:917–25.

[16] Sphaier LA, Worek WM. Parametric analysis of heat and mass transfer regenerators using a generalized effectiveness–NTU method. Int J Heat Mass Transfer 2009;52:2265–72.

[17] Dallaire J, Gosselin L, da Silva AK. Conceptual optimization of a rotary heat exchanger with a porous core. Int J Therm Sci 2010;49:454–62.

[18] Jia CX, Dai YJ, Wu JY, Wang RZ. Use of compound desiccant to develop high performance desiccant cooling system. Int J Refrig 2007;30:345–53.

[19] Simonson CJ, Besant RW. Heat and moisture transfer in energy wheels during sorption, condensation, and frosting conditions. ASME J Heat Transfer 1998;120:699–708.

[20] Sphaier LA, Worek WM. Analysis of heat and mass transfer in porous sorbents used in rotary regenerators. Int J Heat Mass Transfer 2004;47:3415–30.

[21] Zhang LZ, Niu JL. Indoor humidity behaviors associated with decoupled cooling in hot and humid climates. Build Environ 2003;38:99–107.

[22] Zhang LZ, Niu JL. Performance comparisons of desiccant wheels for air dehumidification and enthalpy recovery. Appl Therm Eng 2002;22:1347–67.

[23] Niu JL, Zhang LZ. Effects of wall thickness on the heat and moisture transfers in desiccant wheels for air dehumidification and enthalpy recovery. Int Commun Heat Mass Transfer 2002;29:255–68.

[24] Niu JL, Zhang LZ, Zuo HG. Energy savings potential of chilled-ceiling combined with desiccant cooling in hot and humid climates. Energy Build 2002;34:487–95.

[25] Vali A, Simonson CJ, Besant RW, Mahmood G. Numerical model and effectiveness correlations for a run-around heat recovery system with combined counter and cross flow exchangers. Int J Heat Mass Transfer 2009;52:5827–40.

[26] Li M, Simonson CJ, Besant RW, Mahmood G. Run-around energy recovery system for air-to-air applications using cross-flow exchangers coupled with a porous solid desiccant-part I: model development and verification. HVAC&R Res 2009;15:537–59.

[27] Riffat SB, Zhao X, Doherty PS. Application of sorption heat recovery systems in heating appliances-feasibility study. Appl Therm Eng 2006;26:46–55.

[28] Yuan WX, Zheng Y, Liu XR, Yuan XG. Study of a new modified cross-cooled compact solid desiccant dehumidifier. Appl Therm Eng 2008;28:2257–66.

[29] Zhang LZ. A three-dimensional non-equilibrium model for an intermittent adsorption cooling system. Sol Energy 2000;69:27–35.

[30] Rose J, Nielsen TR, Kragh J, Svendsen S. Quasi-steady-state model of a counter-flow air-to-air heat-exchanger with phase change. Appl Energy 2008;85:312–25.

[31] Liu JJ, Li WS, Liu J, Wang B. Efficiency of energy recovery ventilator with various weathers and its energy saving performance in a residential apartment. Energy Build 2010;42:43–9.

[32] Zhong K, Kang YM. Applicability of air-to-air heat recovery ventilators in China. Appl Therm Eng 2009;29:830–40.

[33] Liu S, Zhao X, Riffat S, Yuan Y. Theoretical and experimental investigations of a liquid desiccant filmed cellulose fibre heat and mass exchanger. Int J Energy Res 2009;33:1076–88.

[34] Kistler KR, Cussler EL. Membrane modules for building ventilation. Chem Eng Res Des 2002;80:53–64.

[35] Min JC, Su M. Performance analysis of a membrane-based enthalpy exchanger: effects of the membrane properties on the exchanger performance. J Membr Sci 2010;348:376–82.

[36] Hu T, Min JC, Song YZ. Modeling and analysis of dynamic adsorption during gas transport through a membrane. J Membr Sci 2009;339:204–8.

[37] Zhang LZ. Investigation of moisture transfer effectiveness through a hydrophilic polymer membrane with a field and laboratory emission cell. Int J Heat Mass Transfer 2006;49:1176–84.

[38] Zhang LZ. Evaluation of moisture diffusivity in hydrophilic polymer membranes: a new approach. J Membr Sci 2006;269:75–83.

[39] Niu JL, Zhang LZ. Membrane-based enthalpy exchanger: material considerations and clarification of moisture resistance. J Membr Sci 2001;189:179–91.

[40] Zhang LZ, Niu JL. Laminar fluid flow and mass transfer in a standard field and laboratory emission cell (FLEC). Int J Heat Mass Transfer 2003;46:91–100.

[41] Zhang LZ, Niu JL. Mass transfer of volatile organic compounds from painting material in a standard field and laboratory emission cell (FLEC). Int J Heat Mass Transfer 2003;46:2415–23.

[42] Zhang LZ. Mass diffusion in a hydrophobic membrane humidification/dehumidification process: the effects of membrane characteristics. Sep Sci Technol 2006;41:1565–82.

[43] Zhang LZ. A fractal model for gas permeation through porous membranes. Int J Heat Mass Transfer 2008;51:5288–95.

[44] Zhang LZ, Niu JL. Effectiveness correlations for heat and moisture transfer processes in an enthalpy exchanger with membrane cores. ASME J Heat Transfer 2002;124:922–9.

[45] Zhang LZ. Heat and mass transfer in a cross flow membrane-based enthalpy exchanger under naturally formed boundary conditions. Int J Heat Mass Transfer 2007;50:151–62.

[46] Zhang LZ, Liang CH, Pei LX. Heat and moisture transfer in application-scale parallel-plates enthalpy exchangers with novel membrane materials. J Membr Sci 2008;325:672–82.

[47] Zhang LZ, Wang YY, Wang CL, Xiang H. Synthesis and characterization of a PVA/LiCl blend membrane for air dehumidification. J Membr Sci 2008;308:198–206.

[48] Zhang LZ. Numerical study of heat mass transfer in an enthalpy exchanger with a hydrophobic–hydrophilic composite membrane core. Numer Heat Transfer A – Appl 2007;51:697–714.

[49] Zhang LZ. Fabrication of a lithium chloride solution based composite supported liquid membrane and its moisture permeation analysis. J Membr Sci 2006;276:91–100.

[50] Zhang LZ, Xiao F. Simultaneous heat and moisture transfer through a composite supported liquid membrane. Int J Heat Mass Transfer 2008;51:2179–89.

[51] Zhang LZ. Heat and mass transfer in a total heat exchanger: cross-corrugated triangular ducts with composite supported liquid membrane. Numer Heat Transfer A – Appl 2008;53:1195–210.

[52] Zhang LZ. Effects of membrane parameters on performance of vapor permeation through a composite supported liquid membrane. Sep Sci Technol 2006;41:3517–38.

[53] Zhang LZ. Coupled heat and mass transfer through asymmetric porous membranes with finger-like macrovoids structure. Int J Heat Mass Transfer 2009;52:751–9.

[54] Zhang LZ, Liang CH, Pei LX. Conjugate heat and mass transfer in membrane-formed channels in all entry regions. Int J Heat Mass Transfer 2010;53:815–24.

[55] Niu JL, Zhang LZ. Heat transfer and friction coefficients in corrugated ducts confined by sinusoidal and arc curves. Int J Heat Mass Transfer 2002;45:571–8.

[56] Zhang LZ, Niu JL. A numerical study of laminar forced convection in sinusoidal ducts with arc lower boundaries under uniform wall temperature. Numer Heat Transfer A – Appl 2001;40:55–72.

[57] Zhang LZ. Heat and mass transfer in plate-fin enthalpy exchangers with different plate and fin materials. Int J Heat Mass Transfer 2009;52:2704–13.

[58] Zhang LZ. Heat and mass transfer in plate-fin sinusoidal passages with vapor-permeable wall materials. Int J Heat Mass Transfer 2008;51:618–29.

[59] Zhang LZ. Thermally developing forced convection and heat transfer in rectangular plate-fin passages under uniform plate temperature. Numer Heat Transfer A – Appl 2007;52:549–64.

[60] Zhang LZ. Laminar flow and heat transfer in plate-fin triangular ducts in thermally developing entry region. Int J Heat Mass Transfer 2007;50:1637–40.

[61] Zhang LZ. Turbulent three-dimensional air flow and heat transfer in a cross-corrugated triangular duct. ASME J Heat Transfer 2005;127:1151–8.

[62] Zhang LZ. Convective mass transport in cross-corrugated membrane exchangers. J Membr Sci 2005;260:75–83.

[63] Zhang LZ. Numerical study of periodically fully developed flow and heat transfer in cross-corrugated triangular channels in transitional flow regime. Numer Heat Transfer A – Appl 2005;48:387–405.

[64] Zhang LZ. An analytical solution for heat mass transfer in a hollow fiber membrane based air-to-air heat mass exchanger. J Membr Sci 2010;360:217–25.

[65] Zhang LZ. Performance deteriorations from flow maldistribution in air-to-air heat exchangers: a parallel-plates membrane core case. Numer Heat Transfer A – Appl 2009;56:746–63.

[66] Zhang LZ. Flow maldistribution and performance deteriorations in a membrane-based heat and mass exchanger. ASME J Heat Transfer 2009;131:111801-1–1-7.

[67] Zhang LZ. Flow maldistribution and thermal performance deterioration in a cross-flow air to air heat exchanger with plate-fin cores. Int J Heat Mass Transfer 2009;52:4500–9.

[68] Zhang LZ, Niu JL. A pre-cooling Munters environmental control cooling cycle in combination with chilled-ceiling panels. Energy 2003;28:275–92.

[69] Zhang LZ, Zhu DS, Deng XH, Hua B. Thermodynamic modeling of a novel air dehumidification system. Energy Build 2005;37:279–86.

[70] Zhang LZ. Energy performance of independent air dehumidification systems with energy recovery measures. Energy 2006;31:1228–42.

[71] Liang CH, Zhang LZ, Pei LX. Independent air dehumidification with membrane-based total heat recovery: modeling and experimental validation. Int J Refrig 2010;33:398–408.

[72] Liang CH, Zhang LZ, Pei LX. Performance analysis of a direct expansion air dehumidification system combined with membrane-based total heat recovery. Energy 2010;35:3891–901.

[73] Zhang LZ, Chen ZY. Convective heat transfer in cross-corrugated triangular ducts under uniform heat flux boundary conditions. Int J Heat Mass Transfer 2011;54:597–605.

[74] Zhang LZ. Heat and mass transfer in a quasi-counter flow membrane-based total heat exchanger. Int J Heat Mass Transfer 2010;53:5478–86.

[75] Zhang LZ, Huang SM. Coupled heat and mass transfer in a counter flow hollow fiber membrane module for air humidification. Int J Heat Mass Transfer 2011;54:1055–63.

[76] Zhang LZ. An analytical solution to heat and mass transfer in hollow fiber membrane contactors for liquid desiccant air dehumidification. ASME J Heat Transfer 2011;133:092001-1–1-8.

[77] Zhang LZ. Heat and mass transfer in a randomly packed hollow fiber membrane module: a fractal model approach. Int J Heat Mass Transfer 2011;54:2921–31.

[78] Zhang LZ, Huang SM, Tang K, Pei LX. Conjugate heat and mass transfer in a hollow fiber membrane module for liquid desiccant air dehumidification: a free surface model approach. Int J Heat Mass Transfer, in press. http://dx.doi.org/10.1016/j.ijheatmasstransfer.2012.03.034.

[79] Zhang XR, Zhang LZ, Liu HM, Pei LX. One-step fabrication and analysis of an asymmetric cellulose acetate membrane for heat and moisture recovery. J Membr Sci 2011;366:158–65.

[80] Pei LX, Zhao WJ, Zhang LZ. Preparation and characterization of porous PVDF membranes for dehumidification with PEG as additive. J Appl Polym Sci 2010;118:2696–703.

[81] Pei LX, Lv ZM, Zhang LZ. Selective adsorption of a novel high selective desiccant for prospective use in heat and moisture recovery for buildings. Build Environ 2012;49:124–8.

[82] Zhang LZ, Zhang XR, Miao QZ, Pei LX. Selective permeation of moisture/VOCs through polymer membranes applied for total heat exchangers for indoor air ventilation. Indoor Air, in press. http://dx.doi.org/10.1111/j.1600-0668.2011.00762.x.